

## Saturn's Rings at True Opposition

RICHARD G. FRENCH

Astronomy Department, Wellesley College, Wellesley, MA; rfrench@wellesley.edu

ANNE VERBISCHER

Department of Astronomy, University of Virginia, Charlottesville, VA; verbischer@virginia.edu

HEIKKI SALO

Department of Physical Sciences, University of Oulu, Finland; hsalo@Sun4.oulu.fi

COLLEEN MCGHEE

Astronomy Department, Wellesley College, Wellesley, MA; cmcghee@wellesley.edu

AND

LUKE DONES

Southwest Research Institute, Boulder, CO; luke@boulder.swri.edu

Received 2007 March 9; accepted 2007 May 19; published 2007 June 25

**ABSTRACT.** On 2005 January 14, the Saturn system was observed at true opposition with the planetary camera of the Wide Field Planetary Camera 2 (WFPC2) on the *Hubble Space Telescope*. This was the culmination of nearly a decade of similar *UBVRI* observations, yielding a uniform set of over 400 high spatial resolution and photometrically accurate radial profiles of the rings that spans the full range of ring inclinations and solar phase angles accessible from the Earth. Using a subset of these images at similar effective ring opening angles  $B_{\text{eff}} \sim -23^\circ$ , we measured the normalized ring reflectivity  $I/F$  over broad regions of the A, B, and C rings as a function of solar phase angle and wavelength. There is a strong surge in brightness near opposition. To measure the width and amplitude of the opposition effect, we fitted two models to the observations: a simple four-parameter linear-exponential model and a more complex model (B. Hapke) that incorporates a wavelength-dependent description of the coherent backscatter opposition effect, as well as the shadow-hiding opposition effect by a particulate surface. From fits to the linear-exponential model, the half-width at half-maximum for the rings is  $\sim 0.1^\circ$  at *BVRI* wavelengths, increasing to  $\sim 0.16^\circ$  and  $\sim 0.19^\circ$  for the A and B rings, respectively, in the *U* filter (338 nm). To assess the contribution of the shadowing of ring particles by each other to the opposition surge, we used Monte Carlo simulations of dynamical models of the rings for a variety of optical depths and particle size distributions, both with and without self-gravity. Multiple scattering is very weak at low phase angles, and thus these simulations are nearly wavelength independent. The interparticle shadow-hiding opposition surge increases in strength with ring optical depth and with broadened size distributions. Self-gravity produces wakes that somewhat complicate the picture, because mutual shadowing by wakes is strongly dependent on illumination and viewing geometry. The observed opposition surge in the rings is much stronger and narrower than that caused by interparticle shadowing. We examined regional variations in the opposition surge across the A, B, and C rings using linear-exponential model fits. Some of these are most easily explained on the basis of optical depth, volume filling factor, and the relative width of the particle size distribution. The opposition effect for the A, B, and C rings is substantially narrower than for two nearby icy satellites, Mimas and Enceladus, indicating that they have distinctly different surface properties.

### 1. INTRODUCTION

On 2005 January 14, in a rare cosmic alignment, the Earth passed directly between Saturn and the Sun. Viewed from Saturn, this resulted in a transit of the Earth across the center of the solar disk. From the Earth, this moment provided an opportunity to observe the Saturn system at true opposition. Using

the planetary camera (PC) of the WFPC2 on the *Hubble Space Telescope* (*HST*), we imaged Saturn's rings at near-zero solar phase angle, the culmination of nearly a decade of such observations spanning more than a full Saturn season, beginning shortly after the 1995–1996 ring plane crossings (southern spring on Saturn) and continuing past Saturn's southern summer solstice in 2002. Collectively, these observations provide

a uniform set of high spatial resolution and photometrically accurate radial profiles of the rings over the full range of ring inclinations and solar phase angles accessible from the Earth.

Variations of ring brightness with ring tilt, phase angle, and wavelength reveal both the scattering properties of individual ring particles as well as their collective spatial and size distributions. An important test of our understanding of the physical and dynamical characteristics of Saturn's rings is our ability to account for the strong surge in ring brightness near opposition. As a step toward this goal, we present recent *HST* measurements of the opposition surge of the A, B, and C rings for solar phase angles  $\alpha$  from nearly zero to  $\leq 6.38^\circ$ . In § 2, we briefly summarize previous observations and the *HST* results used for this study. Then in § 3, we develop a suite of models for the opposition surge. We begin by fitting a simple linear-exponential model to the phase-angle-dependent brightness of selected regions in the A, B, and C rings, primarily to quantify the wavelength-dependent width and amplitude of the narrow opposition peak. Next, we fit Hapke (2002) photometric models for the opposition effect, which account for shadow hiding at the surfaces of individual ring particles and for coherent backscatter, the enhancement of the emergent scattered intensity resulting from constructive interference of the incident and scattered waves. To account for shadowing between ring particles, which is neglected in the Hapke (2002) prescription, we compare ring brightness measurements to Monte Carlo ray-tracing predictions based on  $N$ -body dynamical simulations for a variety of ring optical depths and particle size distributions. We then investigate radial variations in the opposition effect across the entire ring system and compare our results with measurements of the opposition effect for Mimas and Enceladus. Finally, in the last section, we discuss our key findings, compare our results to recent findings from *Cassini* observations, and present our conclusions.

## 2. OBSERVATIONS

### 2.1. Previous Results

The strong brightening of Saturn's rings near opposition has been known for many years. Early investigators relied primarily on photodensitometry of photographic plates, with varying results. Franklin & Cook (1965) presented the first detailed analysis of observations of the opposition effect in Saturn's rings, based on a large series of two-color photographic plates obtained in 1959. They found some evidence for a slight wavelength dependence of the phase curve, a finding supported by Irvine & Lane (1973) using observations taken during the 1963 apparition, and by Lumme & Irvine (1976) from an extensive study of over 200 photographic plates obtained during a 30 year period. These purported wavelength trends were contradicted by Lumme et al. (1983), who observed the B ring at small tilt angle  $B \sim 6^\circ$  and found no wavelength dependence for the phase function for phase angles  $\alpha > 0.26^\circ$ . They concluded that the opposition effect resulted from mutual shadowing

of ring particles in a classical many-particles-thick layer, with a very low volume filling factor, although Brahic (1977), Goldreich & Tremaine (1978), and Cuzzi et al. (1979) had established that the rings should be one or only a few particles thick and consequently have a relatively high volume filling factor, a conclusion supported by later, more detailed studies (Salo 1987, 1992; Wisdom & Tremaine 1988; Richardson 1994; Salo et al. 2004; Karjalainen & Salo 2004). Salo & Karjalainen (2003, henceforth SK2003) showed that the apparent contradiction between the observations and the simulations is largely removed when the ring particle size distribution and the dependence of the vertical scale height on particle size are taken into account.

All of the foregoing studies ignored the potentially large contribution of coherent backscatter to the strong opposition surge at very low phase angles. The coherent backscatter opposition effect (CBOE) has been studied extensively, both theoretically and in the laboratory (Akkermans et al. 1988; Shkuratov 1988; Muinonen et al. 1991; Mishchenko 1992; Nelson et al. 2000), and Hapke (2002) developed a detailed model for the bidirectional reflectance of a surface, accounting both for coherent backscatter and shadow hiding due to surface microstructure. The models of CBOE are highly idealized, and thus far, agreement between the theory and experiments has been elusive (see Shepard & Helfenstein 2007 for a review). Poulet et al. (2002) presented the first detailed analysis of high spatial resolution, photometrically precise measurements of the opposition effect in Saturn's rings, using *Hubble Space Telescope* images. They estimated ring particle roughness and porosity by analyzing the observed ring phase curves in terms of intraparticle shadow hiding, multiple scattering, and coherent backscattering, but they ignored mutual shadowing between particles. Their observations were restricted to phase angles  $> 0.3^\circ$  and thus required extrapolation of the steep opposition brightening to zero phase angle, undersampling the narrowest part of the solar phase curve. Here we present *HST* measurements that remedy those limitations by spanning the full range of phase angles visible from the Earth.

### 2.2. *HST* Observations

The viewing and illumination geometry of the *HST* ring observations is illustrated in Figure 1, which shows the variation of the solar phase angle and the Saturnocentric declinations of the Earth ( $B$ ) and Sun ( $B'$ ) over the period of observation. During each of nine apparitions (labeled by *HST* cycle numbers 6–13), we obtained *UBVRI* images of the rings with the WFPC2 PC camera for several *HST* "visits," chosen to sample the full range of accessible solar phase angles, but concentrated near opposition. Table 1 provides additional details about the observations. For each data set, identified by *HST* program ID, cycle number, and visit number, we list the date of each visit, the ring plane opening angles  $B$  and  $B'$ , the effective ring opening angle  $B_{\text{eff}}$  (defined below), the average

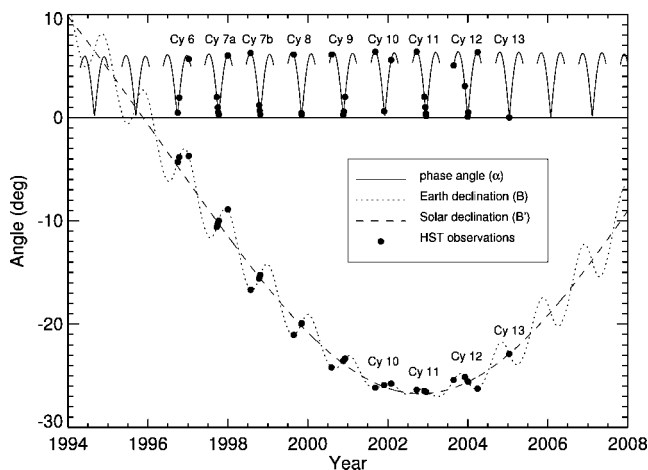


FIG. 1.—Geometry of *HST* observations of Saturn’s rings. The opening angle of the rings as viewed from the Sun (*dashed line*) was nearly zero in 1996, when the first of nine Saturn apparitions was observed using WFPC2. Saturn reached southern summer solstice in late 2002. The ring opening angle as seen from the Earth (*dotted line*) is modulated by the Earth’s annual motion relative to Saturn’s inclined orbit. The solar phase angle is shown at the top of the figure, approaching zero at each opposition and reaching a maximum of just over  $6^\circ$  near quadrature. Filled circles mark the geometric circumstances of the full set of *HST* observations. For this study of the opposition effect, we make use of data from *HST* cycles 10–13, for which the ring opening angle was nearly constant and close to its maximum value as seen from the Earth and the Sun.

solar phase angle  $\alpha$ , and the number of *UBVRI* images taken of the east (E) and west (W) ansae during each visit.<sup>1</sup> Because of the relative inclinations of Earth’s and Saturn’s orbits, the minimum phase angle visible at each opposition was limited to  $\alpha > 0.25^\circ$  for cycles 6–9 and reached  $0.07^\circ$  during cycle 12. During cycle 13 in 2005 January, we observed the rings at true opposition, with  $\alpha \sim 0.01^\circ$ . As discussed below, the finite angular radius of the Sun of  $0.029^\circ$  as seen from Saturn sets an effective lower limit on the phase angle near true opposition.

For each of the more than 400 PC images in our data set, we began with the pipeline-processed data from the Space Telescope Science Institute. We corrected the images for geometric distortion and converted the measured signal to a wavelength-dependent normalized reflectivity  $I/F$ , defined as the ratio of ring surface brightness  $I$  to that of a perfect, flat, Lambert surface at normal incidence  $\pi F(\lambda)/\pi$ , where  $\pi F(\lambda)$  is the solar flux density, or irradiance at Saturn, at wavelength  $\lambda$ . To correct for low-level scattered light, we applied a low-pass deconvolution filter to the data, resulting in a “compensated” image  $(I/F)_{\text{comp}}$ , an approximation to the ideal deconvolved image. The deconvolution procedure has a very minor effect for the

present investigation. For additional details of the complete processing procedure, see Cuzzi et al. (2002).

We used the Encke division as a geometric reference and solved for the center of Saturn in each image. Then, to enable easy comparison of the radial ring profiles, we reprojected each image onto a rectilinear grid  $(r, \theta)$  as a function of ring plane radius  $r$  and ring longitude  $\theta$ , first rebinning each image pixel into  $20 \times 20$  subpixels and then redistributing them into cells in  $(r, \theta)$  with a resolution of 100 km in  $r$  and  $0.1^\circ$  in  $\theta$ . Radial profiles of ring reflectivity  $(I/F)_{\text{corr}}(r)$  were obtained by determining the median value at each  $r$  over a longitude range of  $\pm 5^\circ$  centered on each ring ansa.

As a final step in the processing, we define the geometrically corrected  $I/F$  (see Dones et al. 1993; Cuzzi et al. 2002; French et al. 2007) as

$$(I/F)_{\text{corr}} = \frac{\mu + \mu'}{2\mu'} (I/F)_{\text{comp}}, \quad (1)$$

where  $\mu \equiv |\sin B|$  and  $\mu' \equiv |\sin B'|$ . The effective ring elevation angle  $B_{\text{eff}}$  is defined by

$$\mu_{\text{eff}} \equiv |\sin B_{\text{eff}}| = \frac{2\mu\mu'}{\mu + \mu'}. \quad (2)$$

This correction factor for observations at slightly different  $B$  and  $B'$  is exact for an optically thick, singly scattering, many-particle-thick ring and is a reasonable approximation for multiple scattering (Lumme 1970; Price 1973), although it may be less applicable at very low optical depths. During a single *HST* cycle,  $B_{\text{eff}}$  is roughly constant, although  $B$  and  $B'$  may vary somewhat, as shown in Table 1.

Ring brightness varies with both ring tilt and solar phase angle. Since our primary interest here is in the opposition surge, rather than the well-known “tilt effect” (Cuzzi et al. 2002), we restrict our attention in this paper to data from cycles 10–13. These images sample the full range of available phase angles at nearly the same ring opening angle, minimizing the variations in  $(I/F)_{\text{corr}}$  with ring tilt. Cycles 10–12 were all observed at  $B_{\text{eff}}$  near  $-26^\circ$ , and cycle 13, at  $B_{\text{eff}} = -22.87^\circ$ , is included because these images were acquired at the lowest phase angle of the entire set of observations.

Tables 2–4 present measurements from cycles 10–13 of the average  $(I/F)_{\text{corr}}$  over three ring regions as a function of wavelength (the *UBVRI* filters respectively correspond to WFPC2 filters F336W, F439W, F555W, F675W, and F814W) and solar phase angle.<sup>2</sup> The C ring data (Table 2) are averaged over a radial region (78,000–83,000 km) where the reflectivity is fairly uniform, excluding most of the prominent ringlets and plateaus in this ring. Typical uncertainties in  $(I/F)_{\text{corr}}$  for the C ring are

<sup>1</sup> The field of view of the PC chip of WFPC2 is not large enough to contain the full ring system and its attendant nearby small moons, and we therefore targeted the east and west ring ansae separately during most visits.

<sup>2</sup> The phase angles in Tables 2–4 are measured with respect to the center of the Sun. We account for the Sun’s finite angular size in our models by convolution over the limb-darkened solar image as viewed from Saturn.

TABLE 1  
SUMMARY OF *HST* WFPC2 OBSERVATIONS

PROGRAM ID	CYCLE	VISIT	DATE	$B$	$B'$	$B_{\text{eff}}$	$\alpha$ (deg)	No. of <i>UBVRI</i> Images	
								E	W
6806	6	4	1996 Sep 30	-4.31	-4.73	-4.51	0.46	5	3
6806	6	2	1996 Oct 14	-3.82	-4.93	-4.30	1.93	5	3
6806	6	1	1997 Jan 10	-3.72	-6.25	-4.66	5.67	5	3
7427	7a	2	1997 Sep 22	-10.59	-10.01	-10.29	2.00	5	5
7427	7a	9	1997 Oct 1	-10.28	-10.15	-10.21	0.98	6	5
7427	7a	3	1997 Oct 6	-10.12	-10.22	-10.17	0.50	6	5
7427	7a	4	1997 Oct 10	-9.99	-10.28	-10.13	0.30	5	5
7427	7a	1	1998 Jan 1	-8.88	-11.47	-10.01	6.02	8	5
7427	7b	10	1998 Jul 28	-16.67	-14.38	-15.44	6.26	5	5
7427	7b	64	1998 Oct 13	-15.57	-15.42	-15.49	1.20	5	7
7427	7b	72	1998 Oct 18	-15.43	-15.47	-15.45	0.69	5	5
7427	7b	81	1998 Oct 24	-15.25	-15.56	-15.40	0.32	5	6
8398	8	11	1999 Aug 25	-21.05	-19.36	-20.17	6.11	9	5
8398	8	32	1999 Nov 3	-19.98	-20.16	-20.07	0.43	5	9
8398	8	41	1999 Nov 7	-19.90	-20.20	-20.05	0.30	9	5
8660	9	11	2000 Aug 4	-24.19	-22.92	-23.54	6.10	9	5
8660	9	43	2000 Nov 20	-23.56	-23.83	-23.69	0.27	7	7
8660	9	33	2000 Nov 24	-23.50	-23.85	-23.67	0.59	7	7
8660	9	21	2000 Dec 6	-23.33	-23.96	-23.64	1.99	9	0
8802	10	22	2001 Sep 8	-26.16	-25.71	-25.93	6.37	5	9
8802	10	13	2001 Nov 28	-25.90	-26.07	-25.99	0.62	7	7
8802	10	30	2002 Jan 31	-25.76	-26.29	-26.03	5.58	5	9
9341	11	61	2002 Sep 21	-26.37	-26.73	-26.55	6.38	6	5
9341	11	51	2002 Nov 30	-26.47	-26.72	-26.59	2.01	5	5
9341	11	43	2002 Dec 9	-26.52	-26.72	-26.62	1.00	5	5
9341	11	31	2002 Dec 14	-26.55	-26.71	-26.63	0.40	5	5
9341	11	22	2002 Dec 16	-26.56	-26.71	-26.64	0.23	5	5
9341	11	11	2002 Dec 17	-26.57	-26.71	-26.64	0.15	5	5
9809	12	11	2003 Aug 25	-25.41	-26.17	-25.79	5.05	5	5
9809	12	21	2003 Dec 5	-25.11	-25.75	-25.42	3.05	5	5
9809	12	42	2003 Dec 31	-25.53	-25.61	-25.57	0.08	5	5
9809	12	32	2004 Jan 1	-25.54	-25.61	-25.58	0.10	5	5
9809	12	51	2004 Jan 5	-25.60	-25.59	-25.60	0.50	5	5
9809	12	61	2004 Mar 29	-26.25	-25.11	-25.67	6.34	5	5
10357	13	11	2005 Jan 14	-22.88	-22.87	-22.88	0.01	15	0

$\pm 0.002$  for F555W. For the B ring (Table 3), we averaged over the range 100,000–107,000 km, chosen to avoid the saturated region of the B ring in the F336W cycle 13 zero-phase image. The radial range for the A ring of 127,000–129,000 km (Table 4) was chosen to match the region of maximum observed azimuthal brightness asymmetry in the A ring (French et al. 2007). Typical measurement uncertainties in  $(I/F)_{\text{corr}}$  for the B and A ring data are  $\pm 0.005$  (F555W). The effective wavelengths for each filter, listed in Tables 2–4, were corrected for instrumental response, solar spectrum, and the average ring spectrum (Cuzzi et al. 2002).

### 3. MODELING THE OPPOSITION SURGE

The changing brightness of the rings with phase angle and ring tilt depends on the shadowing of ring particles by each other, the regolith structure of the ring particles themselves, and the degree of multiple scattering, both between ring par-

ticles and within the particles' regolith. A complete description of ring scattering properties would involve a comparison of observations over the full range of solar phase angles and ring tilts, from radio wavelengths to the UV. As a first step, we focus here on quantifying the width and amplitude of the strong and narrow opposition surge itself at visual wavelengths.

#### 3.1. Linear-Exponential Model Fits

We begin with a simple analytic representation of the sharp, narrow opposition surge and the more gradual slope at larger phase angle. Following Poulet et al. (2002) and for eventual comparison with *Cassini* results (Déau et al. 2006; Nelson et al. 2007), we adopt a simple four-parameter combined linear and exponential model commonly used for asteroid and satellite near-opposition phase curves:

$$f(\alpha) = a e^{-\alpha/d} + b + k\alpha, \quad (3)$$

TABLE 2  
C RING: 78,000–83,000 km

F336W		F439W		F555W		F675W		F814W	
$\alpha$	$I/F_{\text{corr}}$								
0.0037	0.0632	0.0046	0.0800	0.0051	0.0845	0.0132	0.0931	0.0126	0.0978
0.0752	0.0546	0.0752	0.0685	0.0752	0.0714	0.0752	0.0799	0.0128	0.0985
0.0753	0.0534	0.0753	0.0668	0.0753	0.0707	0.0753	0.0762	0.0752	0.0842
0.1042	0.0530	0.1043	0.0664	0.1045	0.0729	0.1047	0.0758	0.0754	0.0828
0.1058	0.0524	0.1060	0.0650	0.1061	0.0674	0.1063	0.0743	0.1048	0.0819
0.1477	0.0483	0.1477	0.0609	0.1477	0.0637	0.1476	0.0699	0.1065	0.0786
0.1477	0.0476	0.1477	0.0622	0.1477	0.0660	0.1477	0.0712	0.1476	0.0739
0.2262	0.0447	0.2260	0.0575	0.2258	0.0610	0.2256	0.0650	0.1477	0.0770
0.2274	0.0458	0.2272	0.0593	0.2270	0.0621	0.2268	0.0684	0.2254	0.0706
0.3996	0.0426	0.3994	0.0554	0.3992	0.0579	0.3989	0.0638	0.2266	0.0722
0.4009	0.0413	0.4007	0.0535	0.4005	0.0567	0.4002	0.0605	0.3987	0.0672
0.5002	0.0416	0.5005	0.0543	0.5007	0.0581	0.5010	0.0624	0.4000	0.0654
0.5081	0.0408	0.5084	0.0531	0.5086	0.0588	0.5089	0.0604	0.5012	0.0674
0.6183	0.0409	0.6179	0.0528	0.6176	0.0561	0.6173	0.0604	0.5091	0.0658
0.6201	0.0397	0.6181	0.0529	0.6177	0.0554	0.6191	0.0574	0.6171	0.0655
1.0027	0.0371	0.6197	0.0515	0.6193	0.0538	1.0019	0.0556	0.6189	0.0621
1.0045	0.0366	0.6198	0.0514	0.6195	0.0533	1.0038	0.0539	1.0017	0.0604
2.0113	0.0354	1.0024	0.0486	1.0022	0.0516	2.0106	0.0515	1.0035	0.0585
2.0127	0.0345	1.0042	0.0476	1.0040	0.0500	2.0120	0.0506	2.0104	0.0559
3.0493	0.0331	2.0111	0.0451	2.0109	0.0480	3.0487	0.0507	2.0117	0.0534
3.0511	0.0325	2.0125	0.0439	2.0122	0.0458	3.0504	0.0489	3.0485	0.0550
5.0491	0.0293	3.0491	0.0435	3.0489	0.0483	5.0494	0.0446	3.0502	0.0533
5.0525	0.0304	3.0509	0.0425	3.0507	0.0454	5.0528	0.0474	5.0495	0.0487
5.5758	0.0294	5.0492	0.0386	5.0493	0.0415	5.5761	0.0460	5.0529	0.0514
5.5766	0.0288	5.0526	0.0402	5.0527	0.0436	5.5772	0.0448	5.5762	0.0500
6.3366	0.0288	5.5759	0.0392	5.5760	0.0425	6.3366	0.0437	5.5773	0.0490
6.3369	0.0300	5.5767	0.0384	5.5769	0.0412	6.3368	0.0464	6.3366	0.0477
6.3722	0.0290	5.5767	0.0383	5.5770	0.0408	6.3722	0.0461	6.3368	0.0503
6.3723	0.0279	5.5768	0.0382	5.5771	0.0414	6.3723	0.0440	6.3722	0.0490
6.3758	0.0288	6.3366	0.0376	6.3366	0.0406	6.3757	0.0446	6.3723	0.0469
6.3758	0.0282	6.3369	0.0392	6.3368	0.0440	6.3758	0.0430	6.3757	0.0482
...	...	6.3722	0.0388	6.3722	0.0414	...	...	6.3758	0.0457
...	...	6.3722	0.0387	6.3723	0.0396	...	...	...	...
...	...	6.3722	0.0388	6.3758	0.0412	...	...	...	...
...	...	6.3723	0.0375	6.3758	0.0389	...	...	...	...
...	...	6.3758	0.0379	6.3758	0.0393	...	...	...	...
...	...	6.3758	0.0369	...	...	...	...	...	...

NOTE.— $\lambda_{\text{eff}} = 338, 434, 549, 672, 798$  nm, corresponding to the filters F336W, F439W, F555W, F675W, and F814W, respectively (Cuzzi et al. 2002).

(Piironen et al. 2000; Muinonen et al. 2002; Kaasalainen et al. 2003), where  $f(\alpha)$  is the point-source model  $(I/F)_{\text{corr}}$  at phase angle  $\alpha$ ,  $a$  is the height of the narrow opposition peak,  $b$  is the background intensity,  $d$  is the width of the opposition peak, and  $k$  is the slope of the linear component of the model.

The solar phase angle  $\alpha$  given in Tables 2–4 corresponds to the instantaneous angle between the center of the Sun and the center of the Earth, as seen from Saturn. Terrestrial parallax is completely negligible, and therefore it is not important to take into account the *HST* orbital position at the time of each exposure. However, the Sun is not a point source, and the solar phase angle of the illumination on Saturn's rings varies across the solar disk. An accurate model calculation for the predicted ring brightness thus involves convolving the point-source phase-angle-dependent model brightness over the limb-dark-

ened disk of the solar image. We make use of a simple one-parameter solar limb-darkening model:

$$I_{\lambda}(\hat{r}) = (1 - \hat{r}^2)^{\beta_{\lambda}} \quad (4)$$

(Hestroffer & Magnan 1998), where  $I_{\lambda}(\hat{r})$  is the normalized limb-darkened solar intensity,  $\hat{r}$  is the normalized radial coordinate of the solar disk, and  $\beta_{\lambda}$  is a wavelength-dependent constant chosen to fit the observed solar limb-darkening profile. From Table 2 of Hestroffer & Magnan (1998), we adopt the values  $\beta_{\lambda} = 0.80, 0.65, 0.51, 0.39,$  and  $0.324$  for the *UBVRI* filters, respectively, for all convolutions with the solar image.

We fitted equation (3) to the data in Tables 2–4 for each ring region and filter and computed the model  $(I/F)_{\text{corr}}$  for each observation by convolving over the limb-darkened disk of the

TABLE 3  
B RING: 100,000–107,000 km

F336W		F439W		F555W		F675W		F814W	
$\alpha$	$I/F_{\text{corr}}$								
0.0037	0.3730	0.0046	0.6326	0.0051	0.7915	0.0132	0.8982	0.0126	0.9158
0.0752	0.3447	0.0752	0.5661	0.0752	0.6966	0.0752	0.8081	0.0128	0.9272
0.0753	0.3399	0.0753	0.5612	0.0753	0.7068	0.0753	0.7893	0.0752	0.8263
0.1042	0.3297	0.1043	0.5406	0.1045	0.6996	0.1047	0.7633	0.0754	0.8285
0.1058	0.3273	0.1060	0.5395	0.1061	0.6706	0.1063	0.7691	0.1048	0.8020
0.1477	0.3149	0.1477	0.5290	0.1477	0.6562	0.1476	0.7514	0.1065	0.7866
0.1477	0.3177	0.1477	0.5226	0.1477	0.6593	0.1477	0.7375	0.1476	0.7677
0.2262	0.2989	0.2260	0.5010	0.2258	0.6341	0.2256	0.7086	0.1477	0.7726
0.2274	0.2976	0.2272	0.4987	0.2270	0.6237	0.2268	0.7169	0.2254	0.7408
0.3996	0.2790	0.3994	0.4734	0.3992	0.5956	0.3989	0.6856	0.2266	0.7299
0.4009	0.2797	0.4007	0.4753	0.4005	0.6052	0.4002	0.6766	0.3987	0.6964
0.5002	0.2692	0.5005	0.4618	0.5007	0.5906	0.5010	0.6608	0.4000	0.7078
0.5081	0.2681	0.5084	0.4638	0.5086	0.6076	0.5089	0.6634	0.5012	0.6896
0.6183	0.2647	0.6179	0.4542	0.6176	0.5824	0.6173	0.6546	0.5091	0.6927
0.6201	0.2637	0.6181	0.4538	0.6177	0.5752	0.6191	0.6567	0.6171	0.6835
1.0027	0.2487	0.6197	0.4565	0.6193	0.5848	1.0019	0.6327	0.6189	0.6853
1.0045	0.2484	0.6198	0.4561	0.6195	0.5775	1.0038	0.6322	1.0017	0.6591
2.0113	0.2281	1.0024	0.4345	1.0022	0.5615	2.0106	0.5979	1.0035	0.6585
2.0127	0.2284	1.0042	0.4364	1.0040	0.5631	2.0120	0.6090	2.0104	0.6243
3.0493	0.2125	2.0111	0.4017	2.0109	0.5276	3.0487	0.5770	2.0117	0.6203
3.0511	0.2135	2.0125	0.4043	2.0122	0.5226	3.0504	0.5775	3.0485	0.6024
5.0491	0.1977	3.0491	0.3846	3.0489	0.5223	5.0494	0.5462	3.0502	0.6047
5.0525	0.1970	3.0509	0.3866	3.0507	0.5093	5.0528	0.5449	5.0495	0.5709
5.5758	0.1938	5.0492	0.3624	5.0493	0.4813	5.5761	0.5367	5.0529	0.5701
5.5766	0.1934	5.0526	0.3599	5.0527	0.4780	5.5772	0.5406	5.5762	0.5612
6.3366	0.1881	5.5759	0.3560	5.5760	0.4723	6.3366	0.5284	5.5773	0.5663
6.3369	0.1885	5.5767	0.3587	5.5769	0.4760	6.3368	0.5272	6.3366	0.5541
6.3722	0.1888	5.5767	0.3594	5.5770	0.4705	6.3722	0.5352	6.3368	0.5506
6.3723	0.1897	5.5768	0.3588	5.5771	0.4762	6.3723	0.5380	6.3722	0.5455
6.3758	0.1892	6.3366	0.3457	6.3366	0.4625	6.3757	0.5278	6.3723	0.5490
6.3758	0.1901	6.3369	0.3447	6.3368	0.4725	6.3758	0.5394	6.3757	0.5525
...	...	6.3722	0.3497	6.3722	0.4570	...	...	6.3758	0.5480
...	...	6.3722	0.3486	6.3723	0.4606	...	...	...	...
...	...	6.3722	0.3488	6.3758	0.4623	...	...	...	...
...	...	6.3723	0.3518	6.3758	0.4607	...	...	...	...
...	...	6.3758	0.3469	6.3758	0.4665	...	...	...	...
...	...	6.3758	0.3509	...	...	...	...	...	...

NOTE.— $\lambda_{\text{eff}} = 338, 434, 549, 672, 798$  nm, corresponding to the filters F336W, F439W, F555W, F675W, and F814W, respectively (Cuzzi et al. 2002).

solar image, using

$$\text{model } (I/F)_{\text{corr}} = \frac{\int f(\alpha, \Omega) I_{\lambda}(\Omega) d\Omega}{\int I_{\lambda}(\Omega) d\Omega}, \quad (5)$$

where  $I_{\lambda}(\Omega)$  is the limb-darkened solar intensity,  $\alpha(\Omega)$  is the phase angle, and the integrations are carried out over the solid angle  $d\Omega$  of the solar image as seen from a given point in the rings.

The results of the least-squares fits are given in Table 5. We also include  $a/b$ , the amplitude of the exponential opposition surge  $a$  relative to the mean intensity  $b$ , and the normalized background slope  $k/b$ , corresponding to the fractional change in ring brightness, per degree of phase angle, of the linear term in the model. For comparison with other model fits, we also

list the half-width at half-maximum  $\text{HWHM} = d \ln 2$  and  $R$ , the rms residual between the observed and model  $(I/F)_{\text{corr}}$ . The model fits are plotted in Figure 2 (*left column*) for each ring region. For clarity, the phase angle is shown on a logarithmic scale. A vertical dashed line indicates the angular radius of the solar disk as seen from Saturn, and the flattening of the model curves at smaller phase angles results primarily from the functional form of the model (eq. [3]), and to a lesser extent from convolution with the solar image. The fits are quite acceptable, given the simple form of the four-parameter model function. The models uniformly underestimate the lowest phase angle observations, and the observations at phase angles  $\alpha > 1^\circ$  fall more linearly on these plots than the model curves, but the overall trends are well matched.

The wavelength dependence of the width, amplitude, and slope

TABLE 4  
A RING: 127,000–129,000 km

F336W		F439W		F555W		F675W		F814W	
$\alpha$	$I/F_{\text{corr}}$								
0.0037	0.2790	0.0046	0.4384	0.0051	0.5213	0.0132	0.5791	0.0126	0.5915
0.0752	0.2522	0.0752	0.3847	0.0752	0.4562	0.0752	0.5131	0.0128	0.5991
0.0753	0.2481	0.0753	0.3790	0.0753	0.4583	0.0753	0.4999	0.0752	0.5233
0.1042	0.2420	0.1043	0.3679	0.1045	0.4556	0.1047	0.4854	0.0754	0.5238
0.1058	0.2390	0.1060	0.3629	0.1061	0.4338	0.1063	0.4869	0.1048	0.5106
0.1477	0.2282	0.1477	0.3528	0.1477	0.4212	0.1476	0.4716	0.1065	0.4969
0.1477	0.2276	0.1477	0.3520	0.1477	0.4254	0.1477	0.4656	0.1476	0.4809
0.2262	0.2130	0.2260	0.3333	0.2258	0.4050	0.2256	0.4424	0.1477	0.4863
0.2274	0.2156	0.2272	0.3349	0.2270	0.4016	0.2268	0.4507	0.2254	0.4605
0.3996	0.2010	0.3994	0.3167	0.3992	0.3815	0.3989	0.4282	0.2266	0.4580
0.4009	0.1995	0.4007	0.3155	0.4005	0.3862	0.4002	0.4206	0.3987	0.4374
0.5002	0.1955	0.5005	0.3112	0.5007	0.3809	0.5010	0.4159	0.4000	0.4393
0.5081	0.1925	0.5084	0.3102	0.5086	0.3923	0.5089	0.4150	0.5012	0.4341
0.6183	0.1906	0.6179	0.3055	0.6176	0.3737	0.6173	0.4105	0.5091	0.4333
0.6201	0.1877	0.6181	0.3049	0.6177	0.3705	0.6191	0.4091	0.6171	0.4277
1.0027	0.1789	0.6197	0.3033	0.6193	0.3726	1.0019	0.3919	0.6189	0.4265
1.0045	0.1772	0.6198	0.3035	0.6195	0.3690	1.0038	0.3881	1.0017	0.4097
2.0113	0.1628	1.0024	0.2892	1.0022	0.3570	2.0106	0.3693	1.0035	0.4039
2.0127	0.1619	1.0042	0.2870	1.0040	0.3538	2.0120	0.3746	2.0104	0.3863
3.0493	0.1538	2.0111	0.2664	2.0109	0.3341	3.0487	0.3584	2.0117	0.3795
3.0511	0.1525	2.0125	0.2663	2.0122	0.3290	3.0504	0.3568	3.0485	0.3754
5.0491	0.1403	3.0491	0.2602	3.0489	0.3313	5.0494	0.3381	3.0502	0.3728
5.0525	0.1392	3.0509	0.2564	3.0507	0.3221	5.0528	0.3358	5.0495	0.3523
5.5758	0.1345	5.0492	0.2405	5.0493	0.3061	5.5761	0.3229	5.0529	0.3510
5.5766	0.1332	5.0526	0.2377	5.0527	0.3015	5.5772	0.3225	5.5762	0.3378
6.3366	0.1305	5.5759	0.2299	5.5760	0.2912	6.3366	0.3188	5.5773	0.3379
6.3369	0.1314	5.5767	0.2300	5.5769	0.2910	6.3368	0.3177	6.3366	0.3331
6.3722	0.1336	5.5767	0.2298	5.5770	0.2872	6.3722	0.3267	6.3368	0.3331
6.3723	0.1333	5.5768	0.2298	5.5771	0.2915	6.3723	0.3270	6.3722	0.3339
6.3758	0.1339	6.3366	0.2242	6.3366	0.2866	6.3757	0.3226	6.3723	0.3342
6.3758	0.1336	6.3369	0.2228	6.3368	0.2920	6.3758	0.3301	6.3757	0.3383
...	...	6.3722	0.2292	6.3722	0.2864	...	...	6.3758	0.3357
...	...	6.3722	0.2289	6.3723	0.2885	...	...	...	...
...	...	6.3722	0.2291	6.3758	0.2900	...	...	...	...
...	...	6.3723	0.2303	6.3758	0.2894	...	...	...	...
...	...	6.3758	0.2273	6.3758	0.2927	...	...	...	...
...	...	6.3758	0.2303	...	...	...	...	...	...

NOTE.— $\lambda_{\text{eff}} = 338, 434, 549, 672, 798$  nm, corresponding to the filters F336W, F439W, F555W, F675W, and F814W, respectively (Cuzzi et al. 2002).

of the linear-exponential model fits is shown in Figure 3. For the optically thin C ring, the HWHM of the narrow surge (Fig. 3a) is nearly independent of wavelength, with an average value of  $0.10^\circ$ . In contrast, at F336W the B ring HWHM ( $0.192^\circ$ ) is nearly double that for F555W ( $0.099^\circ$ ) and longer wavelengths; the A ring is an intermediate case, also showing a wider surge in the *U* filter ( $0.158^\circ$ ) than the average value ( $0.09^\circ$ ) at longer wavelengths. The amplitude  $a/b$  (Fig. 3b) has a weak wavelength dependence, with the dark and optically thin C ring showing the strongest opposition surge ( $a/b \approx 0.6$ ), and the opaque B ring the weakest ( $a/b \approx 0.4$ ). The normalized slope (Fig. 3c) shows a similar pattern, with steeper slopes at short wavelengths and generally weaker slopes for the more opaque ring regions. We return to these results below.

We find that the opposition surge is much narrower ( $\sim 0.1^\circ$ –

$0.2^\circ$  HWHM) than Poulet et al. (2002) derived from their analysis of *HST* observations during the 1997–1998 apparition. For the A, B, and C rings, they obtained HWHMs ranging from  $0.41^\circ$  to  $0.67^\circ$ , with no clear wavelength dependence. However, the minimum phase angle of their observations was  $0.3^\circ$ , substantially greater than for our data (see Table 1). From fits to subsets of our current measurements, we find that the fitted HWHM of the narrow opposition surge depends quite strongly on the inclusion of the 2005 January 14 measurements obtained at true opposition. When these observations were excluded from the fits, the HWHM increased from  $0.1^\circ$ – $0.2^\circ$  to  $0.16^\circ$ – $0.25^\circ$ . Similarly, when we fitted only data for which  $\alpha > 0.3^\circ$ , the HWHM ranged from  $0.33^\circ$ – $0.39^\circ$ ,  $0.41^\circ$ – $0.56^\circ$ , and  $0.36^\circ$ – $0.49^\circ$  for the C, B, and A rings, respectively, roughly comparable to the Poulet et al. (2002) results from *HST* measurements at

TABLE 5  
LINEAR-EXPONENTIAL MODEL PARAMETERS FOR SATURN'S RINGS

Ring	Filter	$a$	$b$	$d$ (deg)	$k$ (deg <sup>-1</sup> )	$a/b$	$k/b$	HWHM <sup>a</sup> (deg)	$R^b$
C	F336W	0.025	0.040	0.159	-0.0018	0.625	-0.046	0.110	0.0012
	F439W	0.029	0.052	0.157	-0.0022	0.556	-0.043	0.109	0.0016
	F555W	0.030	0.055	0.154	-0.0023	0.552	-0.042	0.107	0.0021
	F675W	0.036	0.059	0.148	-0.0023	0.613	-0.040	0.103	0.0022
	F814W	0.039	0.064	0.133	-0.0026	0.609	-0.041	0.092	0.0022
B	F336W	0.119	0.252	0.278	-0.0102	0.473	-0.041	0.192	0.0044
	F439W	0.178	0.452	0.186	-0.0167	0.395	-0.037	0.129	0.0085
	F555W	0.217	0.586	0.143	-0.0200	0.370	-0.034	0.099	0.0105
	F675W	0.257	0.657	0.143	-0.0206	0.391	-0.031	0.099	0.0116
	F814W	0.269	0.686	0.131	-0.0221	0.392	-0.032	0.091	0.0103
A	F336W	0.095	0.184	0.228	-0.0084	0.515	-0.046	0.158	0.0039
	F439W	0.140	0.305	0.143	-0.0128	0.457	-0.042	0.099	0.0065
	F555W	0.157	0.376	0.133	-0.0143	0.419	-0.038	0.092	0.0080
	F675W	0.183	0.411	0.134	-0.0145	0.444	-0.035	0.093	0.0082
	F814W	0.193	0.429	0.120	-0.0155	0.450	-0.036	0.083	0.0076

NOTE.— $\lambda_{\text{eff}} = 338, 434, 549, 672, 798$  nm, corresponding to the filters F336W, F439W, F555W, F675W, and F814W, respectively (Cuzzi et al. 2002).

<sup>1</sup> HWHM = half-width at half-maximum.

<sup>2</sup>  $R$  = rms residual of  $(I/F)_{\text{corr}}$ .

smaller  $B_{\text{eff}}$  ( $\sim -10^\circ$ ) than our present data set. These results show that the true opposition measurements are substantially brighter than a simple extrapolation to low phase angles from higher phase observations would suggest, and that the near-zero phase measurements provide a strong constraint on the actual width of the opposition surge.

### 3.2. Hapke Model Fits

The linear-exponential model has the virtue of analytic simplicity, providing useful estimates of the amplitude and the width of the core of the opposition surge itself, as well as the more gradual decline characteristic of the observations at larger phase angles. We next turn to the Hapke (2002) model, which incorporates a wavelength-dependent CBOE based on the theoretical predictions of Akkermans et al. (1988) and an explicit representation of the shadow-hiding opposition effect (SHOE) by a particulate surface. The Hapke (2002) model has been applied to satellite measurements from these same *HST* observations (Verbiscer et al. 2007) and combined with *Voyager* spacecraft measurements (Verbiscer et al. 2005) to quantify the opposition surge on Saturn's satellites, which brighten considerably at true opposition (Verbiscer et al. 2007).

For each ring and filter in Tables 2–4, we fitted the Hapke (2002) model using the nonlinear least-squares algorithm developed by Helfenstein (1986) and described by Helfenstein et al. (1991), modified to accommodate anisotropic multiple scattering as described by Verbiscer et al. (2005). Our model fits appear in the right-hand column of Figure 2, and all parameters derived from the fits are listed in Table 6. These fits have consistently lower rms residuals per degree of freedom than the linear-exponential fits, and they do a better job of capturing both the very low phase angle measurements and the falloff

in  $(I/F)_{\text{corr}}$  for  $\alpha > 1^\circ$ , which is more gradual than implied by the linear-exponential model.

The Hapke (2002) model is characterized by parameters that include the single-scattering albedo  $\omega_0$ , the single-particle phase function asymmetry parameter  $g$ , and the width  $h$  and amplitude  $B_0$  of the SHOE and CBOE. For completeness, we also account for the mean topographic slope angle  $\bar{\theta}$ , using the formalism of Hapke (1984, 1993), which was derived for any general reflectance function. Although the phase angle coverage of the *HST* observations ( $\alpha = 0.01^\circ$ – $6.4^\circ$ ) is well suited to constrain the angular widths of both the SHOE and CBOE, the restriction to Earth-based measurements somewhat compromises our ability to determine parameters such as  $g$  and  $\bar{\theta}$ , which are constrained primarily by data obtained at larger phase angles. As noted by Shepard & Helfenstein (2007), photometric roughness tends to decrease with increasing albedo. This trend is evident in the B ring, for which  $\bar{\theta}$  falls off from  $\sim 41^\circ$  at short wavelengths to  $\sim 27^\circ$  at longer wavelengths, where the albedo is higher. At 549 nm, we find that the roughness of all rings is higher than that determined by Poulet et al. (2002) for the C ring and for Mimas ( $\bar{\theta} = 30^\circ$ ; Verbiscer & Veverka 1992), the innermost of Saturn's "classical" satellites. Our values of  $\bar{\theta}$  are significantly lower than those ( $\bar{\theta} \sim 60^\circ$ – $70^\circ$ ) determined by Poulet et al. (2002); however, no firm conclusions about the roughness of ring particles can be drawn from fits to observations made at phase angles no larger than  $\alpha = 6.4^\circ$ .

The wavelength dependence of several Hapke (2002) model parameters is shown in Figure 3. The single-scattering albedo  $\omega_0$  increases with wavelength for all rings (Fig. 3d), although the increase is much more pronounced for the A and B rings than for the C ring. The albedo of the optically thin C ring is much smaller than that of the optically thick A and B rings.

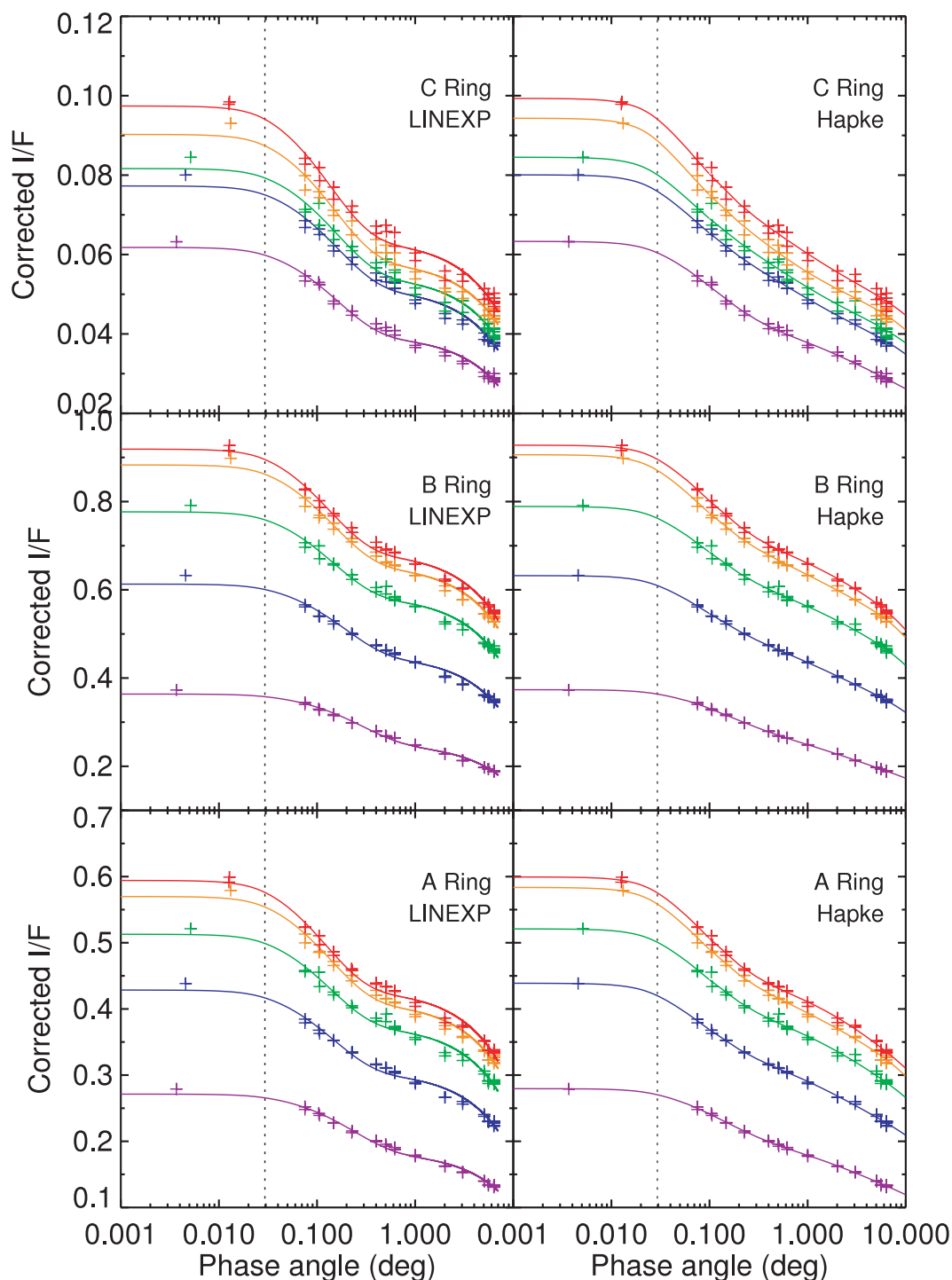


FIG. 2.—Model fits to *HST* WFPC2 observations (Tables 2–4) of the opposition effect for selected regions in Saturn’s C, B, and A rings. The left column shows the results of the linear-exponential (LINEXP) model fits from Table 5, and the right column shows the Hapke (2002) model fits given in Table 6. The colored lines and symbols (*violet to red*) correspond to the F336W, F439W, F555W, F675W, and F814W filters, respectively. The plotted phase angles are measured with respect to the center of the solar image, and the finite size of the Sun was taken into account in the models by convolution over the limb-darkened solar disk (eq. [5]). The vertical dashed lines mark the angular radius of the Sun as viewed from Saturn ( $\alpha_{\text{sun}} = 0.029^\circ$ ), setting the approximate effective minimum solar phase angle of the measurements. The linear-exponential models match the observations reasonably well, given only four free parameters, although they consistently underestimate the lowest ring brightness at minimum phase angle, and they deviate systematically from the measurements near  $\alpha = 0.5^\circ$  (where they underestimate the true ring brightness) and near  $\alpha = 2^\circ$  (where they overestimate the true brightness). The Hapke (2002) models show no such systematic deviations from the measurements.

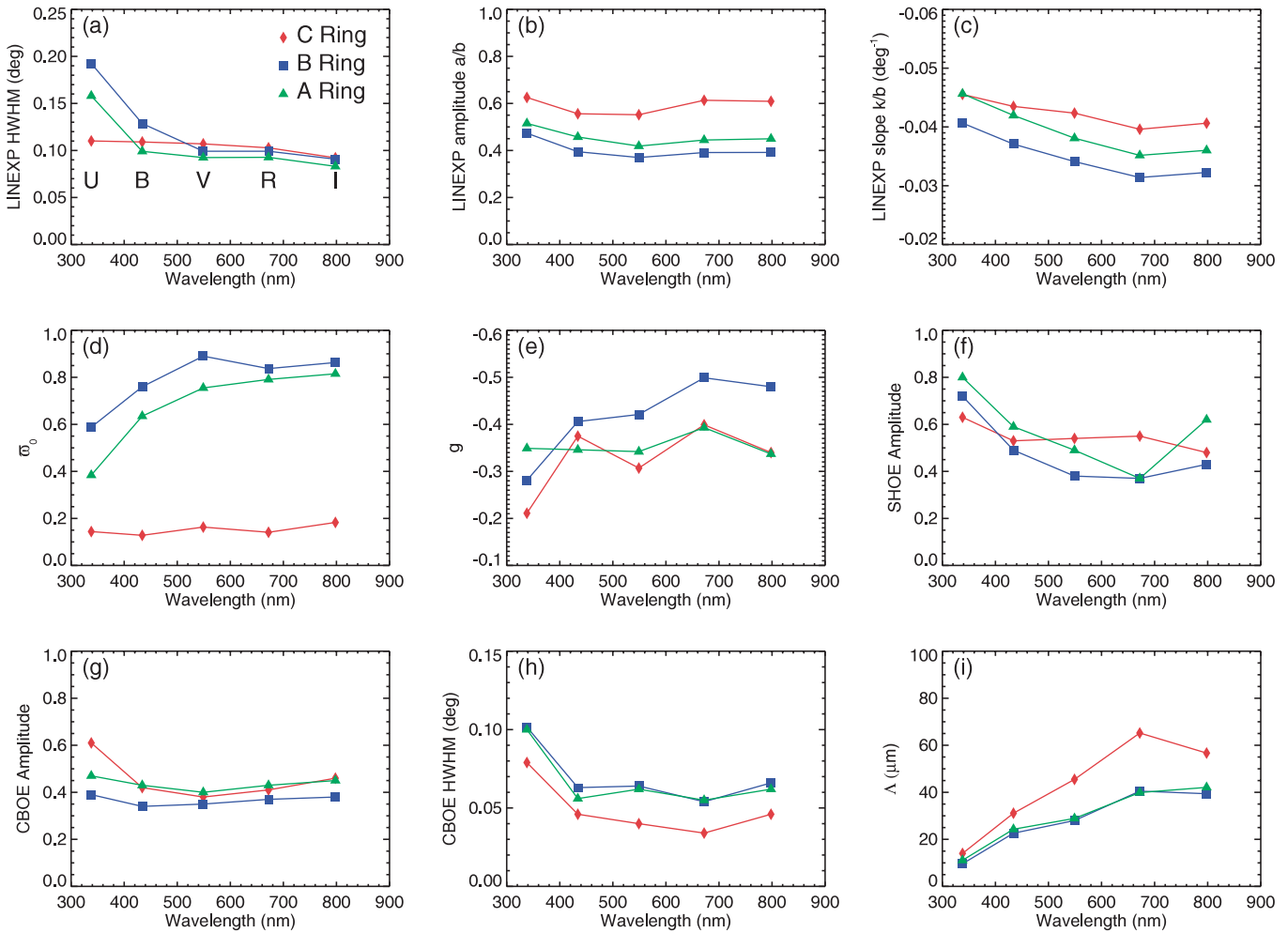


FIG. 3.—Wavelength dependence of linear-exponential (LINEXP) and Hapke (2002) model fits to *HST* WFPC2 observations of the opposition effect for selected regions in Saturn's C, B, and A rings, plotted as a function of the effective wavelength of the WFPC2 *UBVRI* filters. (a)–(c): HWHM, amplitude, and normalized slope from the LINEXP fits (Table 5); (d)–(i): selected parameters from the Hapke (2002) model fits (Table 6).

The asymmetry parameter  $g$  is the average cosine of the scattering angle  $\Theta$ :  $g \equiv \langle \cos \Theta \rangle$  and  $\Theta \equiv \pi - \alpha$ . While  $g$  does not vary significantly with wavelength for the A ring (Fig. 3e), the B ring backscatters more strongly at longer wavelengths, from  $g = -0.28$  at 338 nm to  $g = -0.50$  at 672 nm. Strictly speaking, these model parameters apply to the individual grains in the regolith of a typical ring particle, and not to the particle as a whole.

The transparency of regolith grains affects their ability to cast shadows, and thus the SHOE amplitude (Fig. 3f) is directly related to particle opacity ( $B_{os} = 0$  for transparent particles and  $B_{os} = 1$  for opaque grains). For all rings,  $B_{os}$  generally decreases with wavelength, indicating that particles are more transparent at longer wavelengths. The SHOE angular width  $h_s$  is related to regolith porosity and is only weakly dependent on wavelength, except in the C ring at 338 nm, where it is somewhat higher

than at longer wavelengths (Table 6). If we assume a uniform particle size distribution, then  $h_s = (-3/8) \ln P$ , where  $P$  is the porosity (Hapke 1986). Under this assumption, all of the values of  $h_s$  in Table 6 imply that porosities of ring particle regoliths are very high, ranging from 93% to 99%. The CBOE amplitude  $B_{oc}$  (Fig. 3g) does not show a strong wavelength dependence, except for an increase at short wavelengths for the C ring.

The opacity of regolith grains affects not only the shadowing amplitude, but the width of the coherent backscatter opposition surge as well. According to Hapke (2002), the CBOE HWHM is given by  $0.36\lambda/2\pi\Lambda \approx 0.72h_c$ , where  $\Lambda$  is the transport mean free path, the average distance a photon travels before being deflected by a large angle ( $\sim 1$  rad). In this picture, the CBOE HWHM should increase with wavelength for a constant  $\Lambda$ , but this is not what we see. Instead, we find that the Hapke CBOE HWHM (Fig. 3h) is largest for all rings

TABLE 6  
HAPKE MODEL PARAMETERS FOR SATURN'S RINGS

Ring	Filter	$\varpi_o$	$\bar{\theta}$	$h_s$	$B_{os}$	$h_c$	$B_{cC}$	$g$	$\Lambda$ ( $\mu\text{m}$ )	HWHM (deg)	$R$
C .....	F336W	0.14	41	0.026	0.63	1.92	0.61	-0.21	14.0	0.079	0.0005
	F439W	0.13	47	0.007	0.53	1.11	0.42	-0.38	31.1	0.046	0.0006
	F555W	0.16	49	0.005	0.54	0.96	0.38	-0.31	45.5	0.040	0.0012
	F675W	0.14	48	0.004	0.55	0.82	0.41	-0.40	65.2	0.034	0.0010
	F814W	0.18	44	0.007	0.48	1.12	0.46	-0.34	56.7	0.046	0.0011
B .....	F336W	0.59	40	0.022	0.72	2.80	0.39	-0.28	9.6	0.116	0.0009
	F439W	0.76	41	0.013	0.49	1.53	0.34	-0.41	22.6	0.063	0.0017
	F555W	0.89	43	0.015	0.38	1.55	0.35	-0.42	28.0	0.064	0.0049
	F675W	0.84	29	0.012	0.37	1.32	0.37	-0.50	40.5	0.054	0.0040
	F814W	0.86	26	0.023	0.43	1.61	0.38	-0.48	39.4	0.066	0.0031
A .....	F336W	0.38	37	0.028	0.80	2.43	0.47	-0.35	11.1	0.100	0.0011
	F439W	0.64	40	0.018	0.59	1.42	0.43	-0.35	24.3	0.056	0.0019
	F555W	0.76	43	0.021	0.49	1.51	0.40	-0.34	28.9	0.062	0.0040
	F675W	0.79	47	0.012	0.37	1.34	0.43	-0.39	39.9	0.055	0.0032
	F814W	0.80	33	0.031	0.62	1.51	0.45	-0.34	42.1	0.062	0.0029

NOTES.— $\lambda_{\text{eff}} = 338, 434, 549, 672, 798$  nm, corresponding to the filters F336W, F439W, F555W, F675W, and F814W, respectively (Cuzzi et al. 2002).  $\varpi_o$  = single-scattering albedo ( $\pm 0.02$ ),  $\bar{\theta}$  = macroscopic roughness ( $\pm 4$ ),  $h_s$  = SHOE width ( $\pm 0.003$ ),  $B_{os}$  = SHOE amplitude ( $\pm 0.03$ ),  $h_c$  = CBOE width  $\times 10^3$  ( $\pm 0.03$ ),  $B_{cC}$  = CBOE amplitude ( $\pm 0.07$ ),  $g$  = Henyey-Greenstein asymmetry parameter ( $\pm 0.04$ ),  $\Lambda$  = transport mean free path ( $\pm 0.7$ ), HWHM = CBOE HWHM ( $\pm 0.002$ ), and  $R$  = rms residual.

at the lowest wavelength (338 nm), falling sharply and then remaining relatively constant at  $\sim 0.055^\circ$  with increasing wavelength from 439 to 798 nm. Nelson et al. (2002) suggest that the wavelength dependence of  $h_c$  and the CBOE HWHM may require a broader range of wavelengths than observed here in order to be seen. In addition, Petrova et al. (2007) invoke a third mechanism, the near-field effect, to explain why the predicted spectral behavior of the opposition effect is not observed. The near-field effect is produced by the inhomogeneity of waves in the immediate vicinity of low- to moderate-albedo regolith grains that are comparable in size to the wavelength. If we assume a uniform particle size distribution, according to Helfenstein et al. (1997) we can estimate particle sizes from our Hapke (2002) parameters. The particle radius is given by  $r_p = 3.11\varpi_o(1-g)h_s\Lambda$ , and using the values in Table 6, we find that grains on C ring particles are an order of magnitude smaller ( $r_p \sim 0.16 \mu\text{m}$ ) than those on A and B ring particles. We measure the broadest CBOE widths (and HWHM) where the single-scattering albedo ranges from 0.1 (for the C ring) to 0.6 for the B ring at 338 nm, so it is possible that this third phenomenon may act in addition to coherent backscatter and classical shadow hiding to produce the opposition effect observed in Saturn's rings.

From our Hapke (2002) fits to the *HST* data, we find that the transport mean free path increases with wavelength for all rings, from  $\Lambda \sim 11 \mu\text{m}$  at 338 nm to  $\sim 45 \mu\text{m}$  at 798 nm for the A and B rings, with somewhat higher values in the darker C ring (Table 6, Fig. 3i). Our measurements are consistent with those of Hapke et al. (2006b), who found  $\Lambda \approx 10 \mu\text{m}$  (where the reflectance of the ring was low) to  $\Lambda \approx 40 \mu\text{m}$  (where it was high) in their analysis of *Cassini* VIMS (Visual and In-

frared Mapping Spectrometer) data at wavelengths between 1 and 5  $\mu\text{m}$ . The near-field effect may play an important role here, since it is most efficient in more compact structures of wavelength-sized scatterers at distances comparable to the wavelength, and the transport mean free path is smallest at 338 nm, the shortest wavelength observed, where the albedo of all the rings is low to moderate. A fuller consideration of the interplay of these effects must await additional observations over a broader range of wavelengths and phase angles.

### 3.3. Monte Carlo Simulation of Interparticle Shadowing

The Hapke (2002) model accounts for shadowing within the regolith of a spherical ring particle, but does not explicitly include shadowing between ring particles, which depends on the particle size distribution and the vertical structure of the ring, as well as the slant path optical depth. To assess the importance of interparticle shadowing, we use dynamical simulations in which the optical depth and the width of the size distribution are varied. Although theoretical formulas exist for the mutual shadowing of particles (Lumme & Bowell 1981; Hapke 1986), the advantage of our simulations is that they account for the partial vertical segregation of different particle sizes (SK2003). In these simulations, we adopt the Bridges et al. (1984) formula for the velocity-dependent coefficient of restitution during particle impacts, leading to moderately flattened systems with vertical thickness a few times the diameter of the largest particles (for an illustration, see Fig. 2 in SK2003).

For simplicity, we first concentrated on models that ignore the self-gravity of the rings. We adopted a power-law size

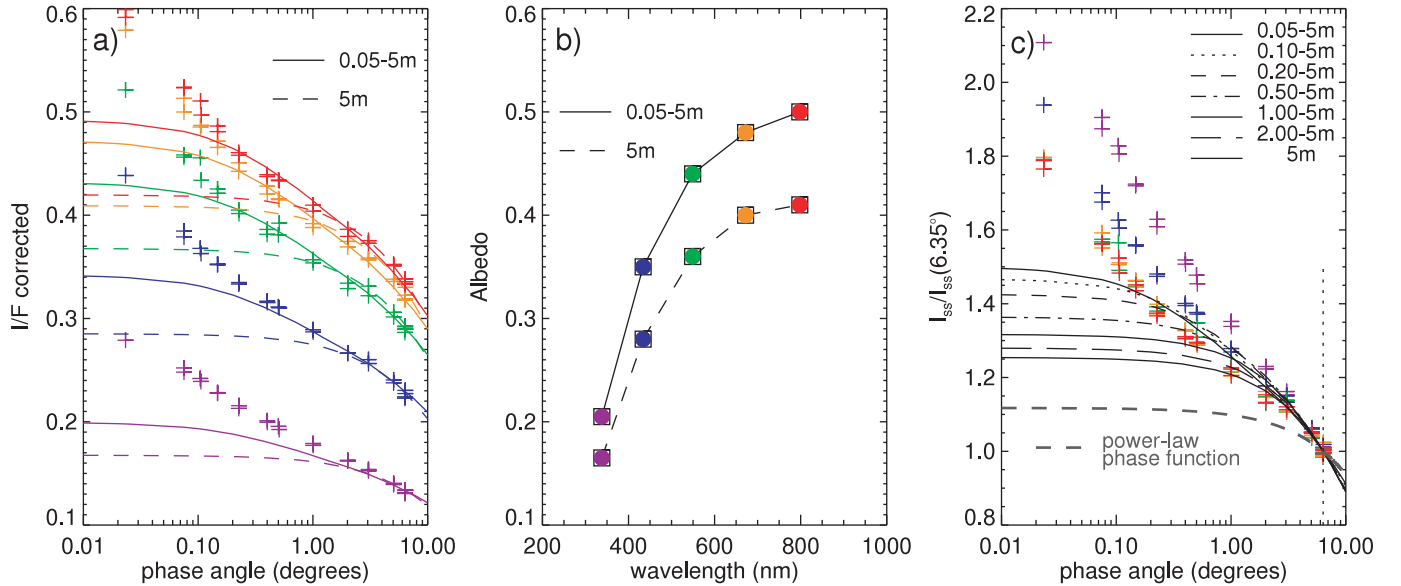


FIG. 4.—Comparison of the observed A ring phase curves (*plus signs*) to the mutual-shadowing opposition effect calculated by photometric Monte Carlo simulations (*curves*). Dynamical simulations with seven different particle size distributions were conducted, ranging from  $q = 3$  power laws for 0.05–5 m to simulations with identical 5 m particles. At left, the two extreme size distribution models are compared to observations at different wavelengths. The single-scattering albedos for the models, indicated in the middle panel, are chosen to fit the observed  $I/F$  at  $\alpha \approx 6^\circ$ . At right, the observations and single-scattering models are normalized to  $\alpha = 6.35^\circ$ . Also shown is the contribution from the adopted power-law phase function alone, amounting to about 1.1 for the interval  $\alpha = 0^\circ$  to  $6.35^\circ$ .

distribution of  $N$  particles with  $dN/dr \propto r^{-q}$  and  $q = 3$ , an upper particle radius cutoff  $r_{\max} = 5$  m, and lower size cutoffs ranging from  $r_{\min} = 0.05$  to 5 m, the latter case corresponding to a monodispersion of identical particles.<sup>3</sup> In each case, the dynamical optical depth  $\tau_{\text{dyn}}$  (the total projected surface area of ring particles per unit area of the rings) was held fixed at 0.5, a typical value for the mid-A ring.

To estimate the contribution of interparticle shadowing to the opposition phase curves, we use a Monte Carlo method based on following a large number of photons through the particle fields produced by the dynamical simulation. The particle field, with periodic planar boundaries, is illuminated by a parallel beam of photons, and the path of each individual photon is followed in detail from one intersection with a particle surface to the next scattering, until the photon escapes the particle field. The new direction after each scattering is obtained via Monte Carlo sampling of the particle phase function. The brightness at the observing direction is obtained by adding together the contributions of all visible individual scatterings. Compared to direct Monte Carlo estimates based on tabulating the directions of escaped photons, this indirect method gives significantly reduced variance. To suppress the statistical fluctuations in the dynamical simulations, we av-

erage the photometric results for several individual simulation snapshots. Because self-gravity was not included, the systems are homogeneous in the planar direction. We consider the effects of self-gravity at the end of this section.

To describe the angular distribution of scattered light from the surface of a ring particle, we adopted a power-law phase function:

$$P_{\text{power}}(\alpha) = c_n(\pi - \alpha)^n, \quad (6)$$

where  $c_n$  is a normalization constant. For  $n = 3.092$ , this gives a good match to the phase function of the inner A ring (Dones et al. 1993); we hereafter refer to this as the power-law phase function. In our Monte Carlo simulations, we take into full account partial shadowing of ring particles by each other, and each scattered photon is followed from its intersection point on the *surface* of a particle (in a direction whose probability is weighted by the power-law phase function), rather than from the particle center. Comparisons of Lambert surface element scattering and Lambert “sphere” scattering (see § 3.5 in SK2003) show the importance of this refinement.

The results of our simulations are shown in Figure 4. In the left panel, we compare the observed  $UBVRI$  A ring phase curves (the data from Table 4, plotted as colored symbols) with the mutual particle shadowing opposition effect calculated from photometric Monte Carlo simulations for two extreme size distributions: a  $q = 3$  power law for 0.05–5 m particles, and a

<sup>3</sup> Although the actual particle size distributions may be somewhat broader in parts of the rings than in these simulations (French & Nicholson 2000), extending the simulations beyond a size range spanning 2 orders of magnitude was computationally prohibitive.

TABLE 7  
 LINEAR-EXPONENTIAL FITS TO DYNAMICAL SIMULATIONS OF FIG. 4

Size (m)	Filter	Albedo	$a$	$b$	$d$ (deg)	$k$ (deg <sup>-1</sup> )	$a/b$	$k/b$	HWHM (deg)	$R$
0.05–5	F336W	0.205	0.034	0.150	0.594	-0.0053	0.225	-0.035	0.412	0.0004
	F439W	0.350	0.057	0.257	0.594	-0.0090	0.223	-0.035	0.412	0.0007
	F555W	0.440	0.072	0.325	0.594	-0.0114	0.222	-0.035	0.412	0.0009
	F675W	0.480	0.079	0.356	0.594	-0.0124	0.221	-0.035	0.412	0.0010
	F814W	0.500	0.082	0.371	0.594	-0.0129	0.221	-0.035	0.412	0.0010
5	F336W	0.165	0.013	0.143	5.070	-0.0039	0.092	-0.027	3.514	0.0001
	F439W	0.280	0.022	0.243	5.071	-0.0066	0.091	-0.027	3.515	0.0001
	F555W	0.360	0.029	0.314	5.072	-0.0084	0.091	-0.027	3.516	0.0001
	F675W	0.400	0.032	0.349	5.073	-0.0094	0.091	-0.027	3.516	0.0001
	F814W	0.410	0.033	0.358	5.073	-0.0096	0.091	-0.027	3.516	0.0001
0.05–5 (ss)	...	...	0.082	0.363	0.594	-0.0129	0.226	-0.036	0.412	0.0010
0.10–5 (ss)	...	...	0.081	0.369	0.959	-0.0118	0.221	-0.032	0.665	0.0005
0.20–5 (ss)	...	...	0.076	0.382	1.463	-0.0114	0.198	-0.030	1.014	0.0003
0.50–5 (ss)	...	...	0.135	0.349	4.470	-0.0047	0.386	-0.014	3.098	0.0002
1.00–5 (ss)	...	...	0.094	0.381	5.316	-0.0088	0.247	-0.023	3.685	0.0002
2.00–5 (ss)	...	...	0.057	0.414	5.466	-0.0113	0.137	-0.027	3.788	0.0002
5 (ss)	...	...	0.040	0.432	5.072	-0.0117	0.092	-0.027	3.516	0.0001

NOTE.—Single-scattering calculations denoted by (ss), HWHM = half-width at half-maximum, and  $R$  = rms residual of fit.

monodispersion of 5 m size particles. The opposition surge for the identical particle case (*dashed lines*) is quite broad, and the  $I/F$  curve is essentially flat for  $\alpha < 1^\circ$ . For the broader size distribution (*solid line*), the surge is narrowed because of the abundance of relatively small particles, not flattening until  $\alpha < 0.1^\circ$ . Following Hapke (1986), this trend can be understood as follows. The angular width of the mutual-shadowing opposition surge is determined by the angular width  $w$  of the typical particle shadow cylinder having length  $L$ :  $w \approx \langle r \rangle / L$ , where  $\langle r \rangle = (\langle \sigma \rangle / \pi)^{1/2}$ , and  $\langle \sigma \rangle$  is the average particle cross section. A typical cylinder has volume  $\langle \sigma \rangle L$  and contains  $\langle \sigma \rangle L n$  particles, where  $n$  is the number density in the scattering layer. Setting this to unity for the shadow cylinder gives  $L = 1 / \langle \sigma \rangle n$ , yielding  $w \approx n \langle \sigma \rangle \langle r \rangle$ , as found by Hapke (1986). In terms of volume density  $D = n \langle V \rangle$ , where  $\langle V \rangle$  is the average particle volume,  $w = \langle \sigma \rangle \langle r \rangle / \langle V \rangle D$ . Thus, the width of the surge is proportional to the volume density, with a proportionality constant that becomes smaller as the width of the size distribution is increased (see Fig. 16 in SK2003).

The Bond albedo for the simulations (Fig. 4b) was chosen to fit the observed  $(I/F)_{\text{corr}}$  at  $\alpha \approx 6^\circ$ . Note that the albedos are higher for the broad size distribution, even though both models assume the same  $\tau_{\text{dyn}}$ . Because the mutual-shadowing opposition effect for identical particles extends to relatively large phase angles (i.e., its angular width is large), a lower albedo is needed to match  $(I/F)_{\text{corr}}$  at  $\alpha \approx 6^\circ$  in this case than for a broad size distribution, where the opposition effect is confined to smaller angles.

The results of Monte Carlo simulations for seven different power-law size distributions are shown in Figure 4c. For simplicity, we ignore multiple scattering, which we show below to be unimportant in this near-backscattering geometry, and

hence these simulations are effectively wavelength independent. Here both the observations and the models are normalized to  $\alpha = 6.35^\circ$ . The contribution to the normalized phase curve from the power-law phase function alone is shown as a dashed line, amounting to about 1.1 for the interval  $\alpha = 0^\circ$  to  $6.35^\circ$ . Clearly, the observed opposition surge is substantially sharper and narrower than the single-particle phase function itself.

To quantify these trends more precisely, we fitted the linear-exponential model (eq. [5]) to the Monte Carlo simulations shown in Figure 4, restricting the phase angle to 25 roughly logarithmically spaced values between  $0^\circ$  and  $6^\circ$ , comparable to the range covered by our Earth-based observations. The results are given in Table 7. For this rather narrow range of phase angles, the fits matched the simulations quite well, as shown by the very small rms error  $R$ . The fitted amplitudes  $a/b$  are nearly independent of albedo (or, equivalently, wavelength), a consequence of the weak contribution made by multiple scattering. For both the 0.05–5 m distribution ( $a/b \approx 0.22$ ) and the 5 m particle size simulations ( $a/b \approx 0.09$ ), the opposition surge amplitude from mutual shadowing is significantly smaller than that of the A ring ( $a/b = 0.419$ – $0.515$ , from Table 5) for comparable  $\tau_{\text{dyn}}$ . The HWHM for the 0.05–5 m case ( $\sim 0.4^\circ$ ) is substantially narrower than the 5 m simulation ( $\sim 3.5^\circ$ ), but neither model matches the A ring's sharp surge with HWHM =  $0.083^\circ$ – $0.158^\circ$  (Table 5). Also included in Table 7 are linear-exponential fit results for the seven normalized single-scattering simulations shown in Figure 4c. The HWHM increases from  $\sim 0.4^\circ$  to  $\sim 3^\circ$  as the width of the particle size distribution is reduced from 2 decades (0.05–5 m) to a single decade (0.5–5 m). Although some jitter is apparent in the trends, due to the intrinsic granularity of the Monte Carlo

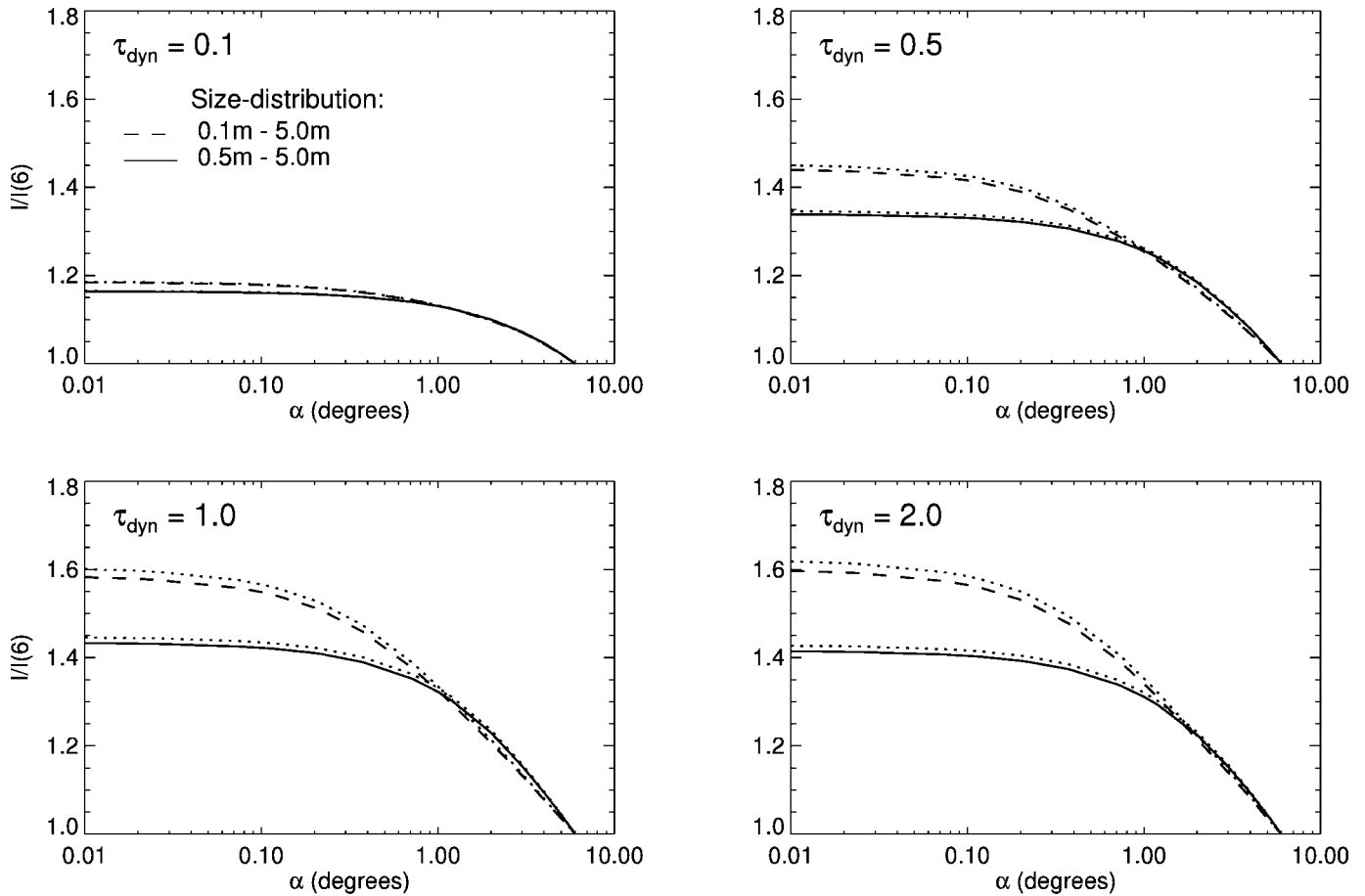


FIG. 5.—Mutual-shadowing near-opposition phase curves, normalized at  $\alpha = 6^\circ$ , from dynamical simulations at four optical depths ( $\tau_{\text{dyn}} = 0.1, 0.5, 1.0,$  and  $2.0$ ) and two  $q = 3$  power-law size distributions: 0.1–5.0 m (*dashed lines*) and 0.5–5.0 m (*solid lines*). The nearby dotted lines show the corresponding single-scattering results. At low optical depths, the opposition surge is quite weak and nearly independent of particle size. For  $\tau_{\text{dyn}} \geq 1$ , the shadow-hiding opposition effect essentially saturates, showing little difference between  $\tau_{\text{dyn}} = 1.0$  and  $2.0$ .

simulations, the expected trend of a narrower and sharper opposition surge for wider size distributions is quite evident.

From these simulations, we find that the long-wavelength (F814W) phase function of the A ring can be matched by mutual particle shadow hiding alone for  $\alpha > 0.2^\circ$  if there is a sufficiently broad size distribution. On the other hand, the F336W phase function in particular is very poorly matched by the interparticle ring-shadowing models for  $\alpha < 1^\circ$ , no matter what particle size distribution is assumed. To investigate the extent to which the mutual-shadowing contribution is affected by ring optical depth, we generated Monte Carlo simulations for  $\tau_{\text{dyn}} = 0.1, 0.5, 1.0,$  and  $2.0$  for two  $q = 3$  size distribution models. As before, we neglected self-gravity and used the Bridges et al. (1984) relation for the coefficient of restitution. We also assumed that  $\varpi_0 = 0.5$  and used the power-law phase function. Figure 5 shows the resulting opposition phase curves, normalized to unity at  $\alpha = 6^\circ$ . At low optical depth ( $\tau_{\text{dyn}} = 0.1$ , typical of the C ring), mutual shadowing is not significant, and the opposition effect is quite weak, barely larger than that

produced by the power-law phase function by itself. With increasing optical depth, the shadow-hiding opposition surge is stronger, reaching saturation for  $\tau_{\text{dyn}} \sim 1.0$ ; note that there is very little difference between the  $\tau_{\text{dyn}} = 1.0$  and  $2.0$  simulation results.

In Figure 5, the phase curves computed for single scattering are shown as dotted lines. At low  $\tau_{\text{dyn}}$ , there is no measurable difference between the single- and multiple-scattering results. As the optical depth increases, multiple scattering slightly reduces the amplitude of the interparticle shadow-hiding opposition surge by filling in the shadows to a small extent. For example, when  $\tau_{\text{dyn}} = 2.0$ , the maximum opposition effect decreases from 1.46 (single scattering only) to 1.44 when multiple scattering is taken into account. Linear-exponential model fits to these simulations are given in Table 8. The key results here are the increasing strength of the mutual shadow-hiding surge with increasing optical depth and broadened size distribution, and the near-insignificance of interparticle multiple scattering at low phase angles.

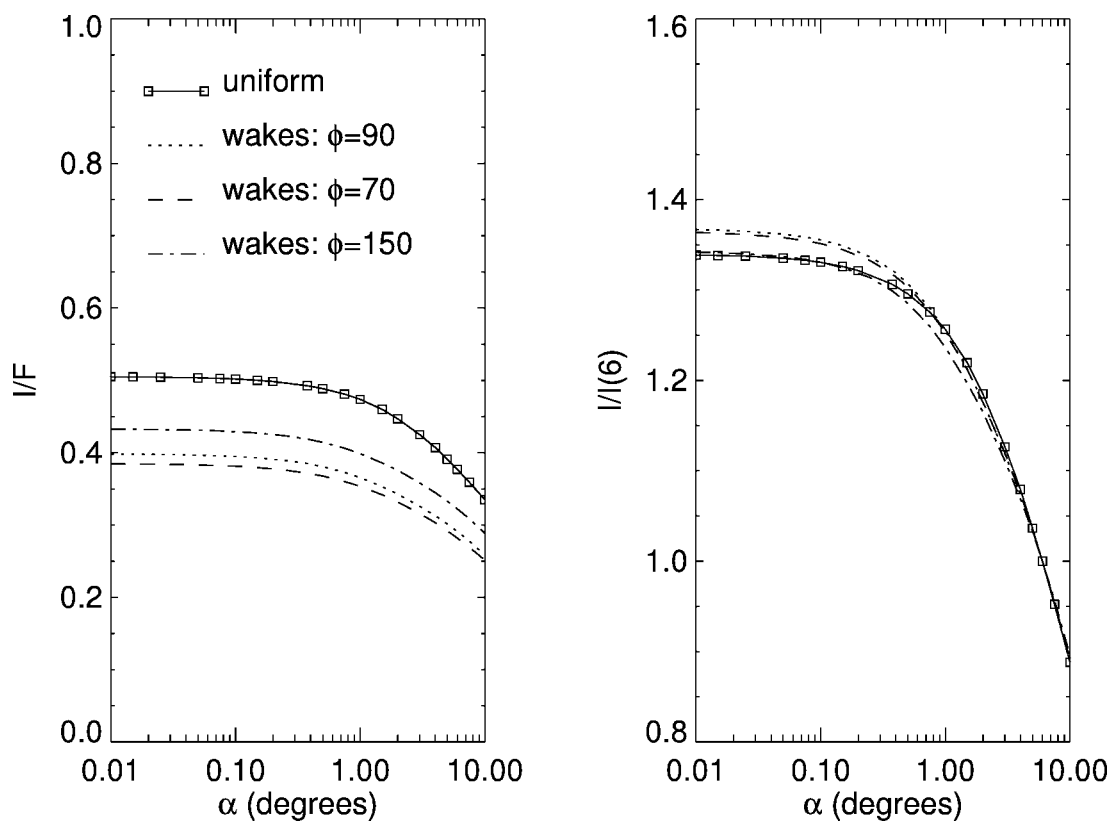


FIG. 6.—Near-opposition phase curves from dynamical simulations of nongravitating (“uniform”) and self-gravitating (“wakes”) particles with  $\tau_{\text{dyn}} = 0.5$  and a 0.5–5 m size distribution, seen at various ring longitudes  $\phi$ . At left, the overall ring brightness varies substantially with viewing geometry, depending on the alignment of the wakes with respect to the observer. The normalized opposition effect itself (*right*) is narrowed somewhat by the presence of wakes caused by self-gravity.

TABLE 8  
LINEAR-EXPONENTIAL FITS TO DYNAMICAL SIMULATIONS OF FIG. 5

$\tau_{\text{dyn}}$	Size (m)	Scattering	$a$	$b$	$d$ (deg)	$k$ ( $\text{deg}^{-1}$ )	$a/b$	$k/b$	HWHM (deg)	$R$
0.10	0.10–5	Multiple	0.051	1.066	1.096	−0.0225	0.048	−0.021	0.760	0.0005
		Single	0.051	1.067	1.099	−0.0227	0.048	−0.021	0.762	0.0005
	0.50–5	Multiple	0.088	1.026	4.703	−0.0169	0.086	−0.016	3.260	0.0001
		Single	0.087	1.027	4.679	−0.0170	0.085	−0.017	3.243	0.0001
0.50	0.10–5	Multiple	0.238	1.101	0.960	−0.0344	0.216	−0.031	0.665	0.0014
		Single	0.243	1.103	0.959	−0.0353	0.221	−0.032	0.665	0.0014
	0.50–5	Multiple	0.357	0.945	4.472	−0.0125	0.378	−0.013	3.100	0.0005
		Single	0.365	0.944	4.470	−0.0128	0.386	−0.014	3.098	0.0005
1.00	0.10–5	Multiple	0.351	1.115	1.007	−0.0398	0.315	−0.036	0.698	0.0019
		Single	0.362	1.119	1.006	−0.0411	0.324	−0.037	0.697	0.0019
	0.50–5	Multiple	0.558	0.861	4.698	−0.0052	0.649	−0.006	3.257	0.0005
		Single	0.571	0.859	4.676	−0.0057	0.664	−0.007	3.241	0.0005
2.00	0.10–5	Multiple	0.367	1.115	1.092	−0.0398	0.329	−0.036	0.757	0.0014
		Single	0.379	1.119	1.092	−0.0412	0.339	−0.037	0.757	0.0014
	0.50–5	Multiple	0.477	0.905	4.592	−0.0113	0.527	−0.012	3.183	0.0002
		Single	0.490	0.903	4.586	−0.0117	0.543	−0.013	3.179	0.0002

NOTE.—HWHM = half-width at half-maximum,  $R$  = rms residual of fit.

TABLE 9  
 LINEAR-EXPONENTIAL FITS TO DYNAMICAL SIMULATIONS OF FIG. 6

Model	$\phi$ (deg)	$a$	$b$	$d$ (deg)	$k$ (deg <sup>-1</sup> )	$a/b$	$k/b$	HWHM (deg)	$R$
Uniform .....	...	0.133	0.358	4.450	-0.0049	0.372	-0.014	3.085	0.0002
Wake .....	70	0.051	0.307	1.714	-0.0088	0.167	-0.029	1.188	0.0004
	90	0.060	0.314	1.875	-0.0084	0.190	-0.027	1.300	0.0004
	150	0.058	0.348	1.747	-0.0091	0.166	-0.026	1.211	0.0004

NOTE.—HWHM = half-width at half-maximum,  $R$  = rms residual of fit.

We have neglected self-gravity in all of the foregoing dynamical simulations, even though it is a crucial ingredient for accurate models of wake structure and azimuthal brightness variations in the rings (SK2003; Salo et al. 2004; French et al. 2007), especially in the A ring. Figure 6 compares the phase curves for nongravitating and self-gravity simulations, seen at various ring longitudes. The average ring brightness in the self-gravitating models varies substantially with viewing geometry, depending on the observer's longitude  $\phi$  (measured in the direction of orbital motion from the subobserver point) relative to the mean wake direction (Fig. 6a). The  $\phi = 70^\circ$  case corresponds to wakes viewed roughly along their long axis. Linear-exponential fits to these simulations (Table 9) show that the phase curves for the wake models are nearly independent of  $\phi$ . However, the amplitude of the surge is weaker when wakes are present ( $a/b = 0.166$ – $0.190$ ) than in the uniform nongravitating case ( $a/b = 0.372$ ), and the width of the shadow-hiding opposition peak is much narrower (HWHM =  $1.188^\circ$ – $1.300^\circ$ ) than for the uniform case (HWHM =  $3.085^\circ$ ). This may be the result of mutual shadowing between wakes, combined with interparticle shadowing. Since the  $3^\circ$  HWHM is nearly half of the full range of phase angles of the observations, broader phase coverage from *Cassini* measurements may be required to derive accurate mutual-shadowing effects in the presence of wakes. These examples illustrate the importance of taking into account the detailed dynamical environment of the rings when interpreting phase curves in terms of ring particle properties.

### 3.4. Regional Variations in the Opposition Surge and Comparison with Icy Satellites

To set the stage for more detailed future models of ring scattering properties, we briefly examine the regional variations in the opposition surge across the A, B, and C rings. For this purpose, we use the linear-exponential model because it has the fewest free parameters and because it provides a reasonably good match to the results of the more elaborate Hapke (2002) formulation (see Figs. 2 and 3). We performed a suite of fits to the complete radial ring brightness profiles for the same *HST* images used for Tables 2–4. Figure 7 shows the amplitude, HWHM, and normalized slope at each wavelength obtained from linear-exponential fits to sliding-box averages of the  $(I/F)_{\text{corr}}$  profiles, binned to a resolution of 300 km in steps of 100 km in radius. For comparison, a representative  $(I/F)_{\text{corr}}$  ring brightness profile and the *Voyager* PPS (Photopolarimeter

Subsystem) optical depth profile, obtained from the NASA Planetary Data System Rings Node (Showalter et al. 1996), are also shown, labeled with the major ring regions.

Overall, there is substantial regional variability in the sharpness, strength, and wavelength dependence of the opposition surge. In the C ring, the detailed variations correlate strongly with the optical depth variations, especially in the inner and outer regions, where there are ringlets and plateaus with abrupt radial changes in opacity. If the surface properties of the C ring particles themselves are uniform, then the CBOE would be expected to be similar throughout the ring, whereas interparticle shadow hiding depends critically on the ring optical depth, particle size distribution, and volume filling factor. The C ring is known to have a relatively broad particle size distribution: French & Nicholson (2000) found  $q = 3.1$ ,  $r_{\text{min}} = 1$  cm,  $r_{\text{max}} = 10$  m. As we have seen, this both narrows and sharpens the shadow-hiding opposition surge. In future work, inclusion of ring observations over a wider range of tilt angles (Salo et al. 2005) will help to disentangle the wavelength-dependent CBOE and shadow hiding in the regolith from interparticle effects.

The opposition effect changes markedly at the boundary between the outer C and inner B rings. Over the radial range 92,000–99,000 km, which is the least opaque part of the B ring, the amplitude exceeds 0.5, decreasing gradually with increasing radius and optical depth. Between 100,000 and 107,000 km (the region used for Table 3 and for our fits in Figs. 2 and 3 and Tables 5 and 6), the normalized slope decreases with increasing ring optical depth. Throughout the B ring, the opposition effect is strongly wavelength dependent, especially at short wavelengths, where the single-scattering albedo is also strongly wavelength dependent.<sup>4</sup> Compared to the C ring, the B ring particle size distribution is relatively narrow in terms of  $r_{\text{max}}/r_{\text{min}}$ :  $q = 2.75$ ,  $r_{\text{min}} = 30$  cm,  $r_{\text{max}} = 20$  m (French & Nicholson 2000). This tends to weaken the interparticle opposition amplitude (Fig. 4), but this is compensated for in part by the enhanced optical depth of the B ring (Fig. 7). Wakelike structure has been observed in regions of the B ring (French et al. 2007; Colwell et al. 2007), and this might also contribute to radial variations in the mutual shadow-hiding component of the opposition effect.

<sup>4</sup> The lone cycle 13 F336W image taken at true opposition was saturated in the range 107,000–118,000 km, resulting in the gap in coverage for that filter in Fig. 7.

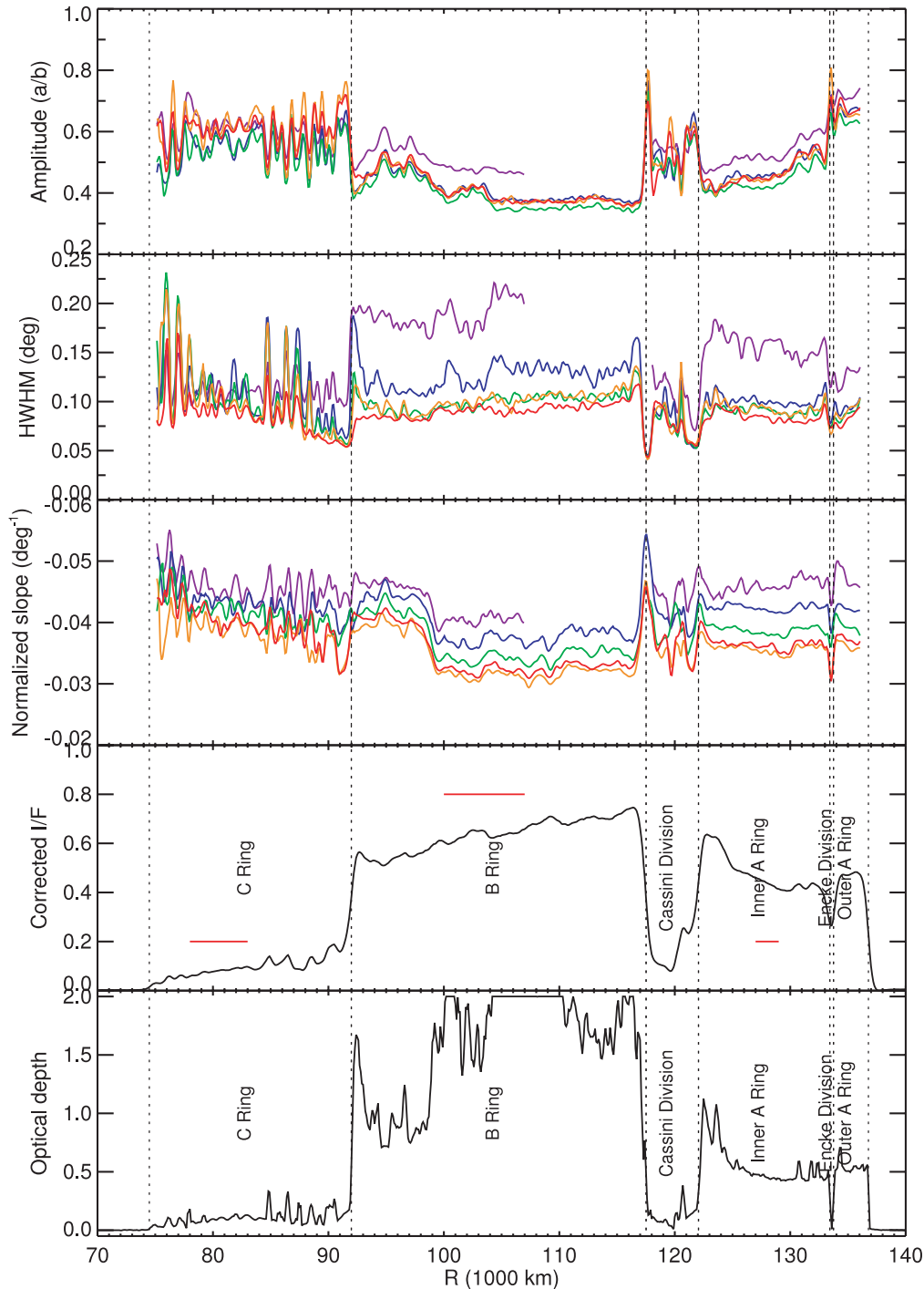


FIG. 7.—Radial variations in the amplitude, width, and slope of the opposition surge from linear-exponential model fits to *HST* WFPC2 observations of Saturn's rings at five wavelengths, taken during cycles 10–13. The colors are the same as in Fig. 2. The amplitude of the opposition effect (*top*) is nearly independent of wavelength, except for the F336W filter (*violet line*), especially in the A and B rings, where the amplitude increases sharply at short wavelengths. (The gap in the F336W profiles between 107,000 and 118,000 km results from saturation of a unique low-phase-angle cycle 13 image, making the model fits unreliable in this region for this filter.) The width of the opposition surge varies strongly with ring region at short wavelengths in the A and B rings, and shows strong correlations with optical depth in the inner and outer C ring. The normalized slope (*third panel*) is most shallow for the optically thick central B ring. A radial profile of ring brightness  $(I/F)_{\text{corr}}$  is shown at bottom from a cycle 13 F439W image taken near true opposition ( $\alpha = 0.0043^\circ$  on 2005 January 14; image u97f1106m). The horizontal red bars demarcate the radial ranges used for Tables 2–4. The bottom panel shows the *Voyager* PPS optical depth profile, truncated at  $\tau = 2.0$  because of limited signal-to-noise ratio at high optical depths.

The Cassini division resembles the C ring in optical depth and possibly in particle size distribution, and these similarities are reflected in the opposition effects of these two separated ring regions. The very strong opposition amplitudes at the inner and outer edges of the Cassini division (Fig. 7) are similar to those in the C ring, and once again there are strong correlations with optical depth variations. Higher resolution *Cassini* images for these two regions will be especially valuable in quantifying these connections.

The A ring and the inner B ring have comparable optical depths, and the overall characteristics of the opposition effect are similar, including significant strengthening and broadening at short wavelengths. The particle size distribution of the inner A ring ( $q = 2.75$ ,  $r_{\min} = 30$  cm,  $r_{\max} = 20$  m; French & Nicholson 2000) is similar as well, and measurements of the strong quadrupole brightness variations (French et al. 2007) indicate that self-gravity wakes are especially strong in the central A ring region. Figure 7 reveals a striking contrast between the inner and outer A ring opposition effect. Outside of the Encke division, the amplitude  $a/b \sim 0.7$ , much larger than anywhere else in the A and B rings and comparable to the largest seen in the C ring. The HWHM is a bit narrower here than in the inner A ring as well. These are just the trends expected from interparticle shadowing for a broad size distribution, and indeed the outer A ring has a much greater abundance of small particles ( $q = 2.9$ ,  $r_{\min} = 1$  cm,  $r_{\max} = 20$  m; French & Nicholson 2000) than the inner A ring.

Verbiscer et al. (2007) used the Hapke (2002) model to describe the opposition effect of Saturn’s icy satellites from the *HST* observations summarized in Table 1, and it is instructive to compare these results with our measurements of the opposition effect of the A, B, and C rings (Fig. 8). Mindful of the possible limitations of the relationship between model parameters and actual microphysical surface textural properties (Shepard & Helfenstein 2007), there are clear differences between the ring and satellite opposition surges, suggesting that they have distinct surface properties. Interpreted in terms of the Hapke (2002) model, we find the following trends. The A, B, and C rings have much smaller SHOE and CBOE widths than those of the icy satellites, and particles in the optically thin C ring have narrower SHOE and CBOE widths than those in the optically thick A and B rings. In general, the CBOE amplitudes for ring particles are comparable to or a bit larger than those for Mimas and Enceladus, the two “classical” Saturnian satellites that orbit closest to the rings. However, the SHOE widths and amplitudes of ring particles are quite distinct from those for icy satellites. The narrower SHOE widths for ring particles suggest that they have higher porosities than icy satellite surfaces. The much larger SHOE amplitudes for the icy satellites imply that particles on Enceladus and Mimas are more opaque than ring particles. Just as both the SHOE and CBOE amplitudes of the darker C ring are higher than those of the bright A and B rings, the SHOE and CBOE amplitudes of the (relatively) darker surface of Mimas are higher than those

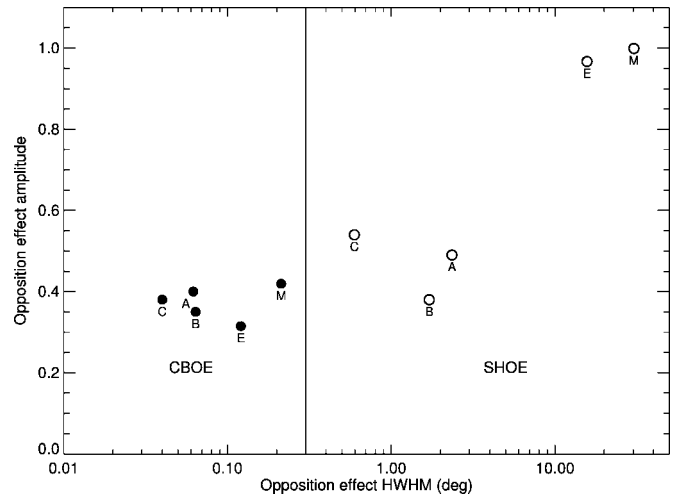


FIG. 8.—Opposition effect amplitude vs. its angular width at half-maximum (HWHM) due to coherent backscatter (filled circles) and shadow hiding (open circles) for Saturn’s A, B, and C rings, Mimas (M), and Enceladus (E) at  $0.55 \mu\text{m}$ . The CBOE of the ring particles is substantially narrower and on average a bit stronger than their icy counterparts. The SHOE of the rings is both weaker and narrower than for Mimas and Enceladus, although this may be affected somewhat by the relatively narrow range of phase angles ( $\alpha < 6.4^\circ$ ) covered by the ring observations.

of Enceladus, implying that C ring particles are more opaque than those in the A and B rings.

#### 4. DISCUSSION AND CONCLUSIONS

We have obtained a set of over 400 uniform, high-resolution *UBVRI* images of Saturn’s rings, taken with the *HST*’s WFPC2 during more than a full Saturn season and over a range of phase angles from  $0.0035^\circ$  to  $6.38^\circ$ . Using a subset of these data at similar ring opening angles ( $B_{\text{eff}} \sim -22.88^\circ$  to  $-26.64^\circ$ ), including high spatial resolution measurements at true opposition, we present photometrically accurate absolute brightness measurements of selected regions in the A, B, and C rings as a function of solar phase angle. The availability of true opposition data allows us to measure the true width and amplitude of the opposition surge without requiring extrapolation to zero phase. The opposition effect is very strong and narrow throughout the rings, substantially narrower than that found by Poulet et al. (2002) from a more restricted set of *HST* measurements limited to  $\alpha > 0.3^\circ$ . There is significant wavelength dependence at the shortest wavelengths, and strong regional variability. To quantify the properties of the opposition surge, we fitted the data using a simple four-parameter linear-exponential model as well as a more complex model (Hapke 2002) that included both intraparticle shadow hiding in the regolith and the coherent backscatter effect. The width of the CBOE at short wavelengths increases rather than decreases, contrary to expectation, although Shepard & Helfenstein (2007) have recently shown from laboratory experiments that one must proceed with cau-

tion when interpreting the results of Hapke model fits in terms of physical properties of a particulate surface.

To complement these models for the opposition effect based on individual ring particle properties, we utilized a variety of dynamical  $N$ -body simulations of the rings, taking into account interparticle shadowing for a range of particle size distributions and optical depths (SK2003; Salo et al. 2004). This component of the overall opposition effect is nearly wavelength independent, owing to the small contribution of interparticle multiple scattering at low phase angles. The amplitude and width of this effect depend strongly on the volume density and size distribution of the ring particles. Simulations including the self-gravity of the ring particles produce aligned wakelike structures and a quadrupole brightness asymmetry in the overall ring brightness, and also slightly decrease both the amplitude and the width of the opposition effect. The observed opposition surge in the rings is much stronger and narrower than that caused by interparticle shadowing alone.

The characteristics of the opposition surge of the rings show substantial regional variations. Some of these are most easily explained on the basis of optical depth and volume filling factor, as well as the local width of the particle size distribution. The presence of wakes in the A and B rings complicates the picture somewhat, because shadowing of wakes by each other is strongly dependent on the viewing and illumination geometries.

The rings' opposition surge differs from that of two nearby icy satellites, Mimas and Enceladus. The rings' CBOE is narrower and a bit stronger than for the satellites, whereas the SHOE component for the rings is both weaker and narrower than for the satellites. Although detailed interpretations are beyond the scope of this work, the clear difference in opposition surge characteristics of the rings and moons indicates that they have distinctly different surface properties.

Recently, direct observations of the opposition effect have been carried out at high resolution by *Cassini* remote-sensing instruments. The Imaging Science Subsystem (ISS) has observed the opposition spot crossing Saturn's rings on several occasions, including a nearly diametric passage in 2005 June. E. Déau et al. (2007, private communication) analyzed 78 images taken in 2005 June ( $B = B' \sim -21^\circ$ ) and 48 images taken in 2006 July ( $B = B' \sim -17^\circ$ ) through the clear filters of the *Cassini* wide-angle camera, whose central wavelength is 635 nm. These images cover phase angle ranges of  $0^\circ$ – $2.5^\circ$ ,  $4^\circ$ – $10^\circ$ , and  $10^\circ$ – $25^\circ$ . For most of their analysis, E. Déau et al. (2007, private communication) use a "linear by parts" model (Lumme & Irvine 1976) in which the rings'  $I/F$  is assumed to vary linearly with phase

angle at very small phase angles, and also linearly, but with a different coefficient, outside the opposition region. Their results are broadly consistent with ours: for example, E. Déau et al. (2007, private communication) find that the opposition surge has the largest amplitude in the C ring and outer A ring. However, they generally find a larger value of HWHM for the surge than we do, even when using a linear-exponential model. The origin of this discrepancy is currently being investigated.

Results from *Cassini* VIMS images at infrared wavelengths have been presented by Nelson et al. (2006), Hapke et al. (2006a, 2006b), and Nelson et al. (2007). They find a strongly wavelength-dependent opposition HWHM, ranging from  $0.2^\circ$  at  $1.5 \mu\text{m}$  to  $>1^\circ$  for  $\lambda > 3.5 \mu\text{m}$ , which they interpret as evidence for a coherent backscatter effect. Their linear-exponential fits are restricted to phase angles  $0.029^\circ < \alpha < 1^\circ$  (R. Nelson 2007, private communication), and as we have shown above, the HWHM values from linear-exponential fits depend rather sensitively on the range of phase angles included in the fits. This may account in part for their larger HWHM than ours, for comparable wavelengths. A more robust comparison between the VIMS findings of a sharply increasing HWHM with wavelength in the IR, and our *HST* results showing that at visual wavelengths, the HWHM is largest at  $U$  and nearly constant at  $VBRI$ , will require careful assessment of such effects.

Our current results, combined with *Cassini* measurements at different wavelengths and under different illumination and viewing conditions, will provide a more complete understanding of the photometric behavior of Saturn's rings. For future studies, it will be important to account for the sharp coherent backscattering opposition surge, as well as for intra- and interparticle shadowing based on realistic dynamical models for the rings with regionally varying particle size distributions.

We would like to thank the staff at STScI, especially Tony Roman and Ron Gilliland, for valuable assistance in planning the *HST* observations, and an anonymous reviewer for a careful reading of the original manuscript and for constructive suggestions. Our results are based on observations with the NASA/ESA *Hubble Space Telescope*, obtained at the Space Telescope Science Institute (STScI), which is operated by the Association of Universities for Research in Astronomy, Inc., under NASA contract NAS 5-26555. This work was supported in part by grants from STScI, by NASA's Planetary Geology and Geophysics program, and by the National Science Foundation and the Academy of Finland.

## REFERENCES

- Akkermans, E., Wolf, P., Maynard, R., & Maret, G. 1988, *J. Phys.*, 49, 77  
 Brahic, A. 1977, *A&A*, 54, 895  
 Bridges, F. G., Hatzes, A., & Lin, D. N. C. 1984, *Nature*, 309, 333  
 Colwell, J. E., Esposito, L. W., Sremčević, M., McClintock, W. E., & Stewart, G. R. 2007, *Icarus*, in press  
 Cuzzi, J. N., Durisen, R. H., Burns, J. A., & Hamill, P. 1979, *Icarus*, 38, 54  
 Cuzzi, J. N., French, R. G., & Dones, L. 2002, *Icarus*, 158, 199  
 Déau, E., Charnoz, S., Dones, L., Brahic, A., & Porco, C. 2006, *AAS Planet. Sci. Meet. Abs.*, 38, 51.01  
 Dones, L., Cuzzi, J. N., & Showalter, M. R. 1993, *Icarus*, 105, 184

- Franklin, F. A., & Cook, F. A. 1965, *AJ*, 70, 704
- French, R. G., & Nicholson, P. D. 2000, *Icarus*, 145, 502
- French, R. G., Salo, H., McGhee, C. A., & Dones, L. 2007, *Icarus*, in press
- Goldreich, P., & Tremaine, S. D. 1978, *Icarus*, 34, 227
- Hapke, B. 1984, *Icarus*, 59, 41
- . 1986, *Icarus*, 67, 264
- . 1993, *Theory of Reflectance and Emittance Spectroscopy* (Cambridge: Cambridge Univ. Press)
- . 2002, *Icarus*, 157, 523
- Hapke, B. W., Nelson, R. M., Smythe, W. D., & Mannatt, K. 2006a, *AAS Planet. Sci. Meet. Abs.*, 38, 62.04
- Hapke, B. W., et al. 2006b, 37th Lunar and Planetary Science Conference, 1466
- Helfenstein, P. 1986, Ph.D. thesis, Brown Univ.
- Helfenstein, P., Hillier, J., Weitz, C., & Veverka, J. 1991, *Icarus*, 90, 14
- Helfenstein, P., Veverka, J., & Hillier, J. 1997, *Icarus*, 128, 2
- Hestroffer, D., & Magnan, C. 1998, *A&A*, 333, 338
- Irvine, W. M., & Lane, A. P. 1973, *Icarus*, 18, 171
- Kaasalainen, S., Piironen, J., Kaasalainen, M., Harris, A. W., Muinonen, K., & Cellino, A. 2003, *Icarus*, 161, 34
- Karjalainen, R., & Salo, H. 2004, *Icarus*, 172, 328
- Lumme, K. 1970, *Ap&SS*, 8, 90
- Lumme, K., & Bowell, E. 1981, *AJ*, 86, 1694
- Lumme, K., & Irvine, W. M. 1976, *AJ*, 81, 865
- Lumme, K., Irvine, W. M., & Esposito, L. W. 1983, *Icarus*, 53, 174
- Mishchenko, M. I. 1992, *Ap&SS*, 194, 327
- Muinonen, K. O., Sihvola, A. H., Lindell, I. V., & Lumme, K. A. 1991, *J. Opt. Soc. Am.* 8, 447
- Muinonen, K., Piironen, J., Kaasalainen, S., & Cellino, A. 2002, *Mem. Soc. Astron. Italiana*, 73, 716
- Nelson, R. M., Hapke, B. W., Smythe, W. D., & Spilker, L. J. 2000, *Icarus*, 147, 545
- Nelson, R. M., Smythe, W. D., Hapke, B. W., & Hale, A. S. 2002, *Planet. Space Sci.*, 50, 849
- Nelson, R. M., et al. 2006, 37th Annual Lunar and Planetary Science Conference, 1461
- Nelson, R. M., & *Cassini* VIMS Rings OE Team 2007, European Geosciences Union General Assembly 2007 (EGU2007-A-05103; Vienna: EGU)
- Petrova, E. V., Tishkovets, V. P., & Jockers, K. 2007, *Icarus*, 188, 233
- Piironen, J., Muinonen, K., Keränen, S., Karttunen, H., & Peltoniemi, J. I. 2000, *Advances in Global Change Research*, Vol. 4. (Netherlands: Kluwer)
- Poulet, F., Cuzzi, J. N., French, R. G., & Dones, L. 2002, *Icarus*, 158, 224
- Price, M. J. 1973, *AJ*, 78, 113
- Richardson, D. C. 1994, *MNRAS*, 269, 493
- Salo, H. 1987, *Icarus*, 70, 37
- . 1992, *Nature*, 359, 619
- Salo, H., & Karjalainen, R. 2003, *Icarus*, 164, 428 (SK2003)
- Salo, H., Karjalainen, R., & French, R. G. 2004, *Icarus*, 170, 70
- Salo, H., French, R. G., McGhee, C., & Dones, L. 2005, *BAAS*, 37, 772
- Shepard, M. K., & Helfenstein, P. 2007, *J. Geophys. Res.*, 112, E03001
- Shkuratov, I. G. 1988, *Kinem. Fiz. Nebe. Tel.* 4, 33
- Showalter, M. R., Bollinger, K. J., Nicholson, P. D., & Cuzzi, J. N. 1996, *Planet. Space Sci.*, 44, 33
- Verbiscer, A. J., & Veverka, J. 1992, *Icarus*, 99, 63
- Verbiscer, A. J., French, R. G., & McGhee, C. A. 2005, *Icarus*, 173, 66
- Verbiscer, A., French, R., Showalter, M., & Helfenstein, P. 2007, *Science*, 315, 815
- Wisdom, J., & Tremaine, S. 1988, *AJ*, 95, 925